Precambrian Research 394 (2023) 107108

Contents lists available at ScienceDirect

Precambrian Research

journal homepage: www.elsevier.com/locate/precamres

Constraints on the age of dome-and-keel structures in the Pilbara Craton through integrated garnet geochronology and microstructural analyses

Ross Salerno [a,*], Nicolas Roberts [b], Jeffrey Vervoort [a], Basil Tikoff [b]

[a] Washington State University, School of the Environment, Pullman, WA, United States
[b] University of Wisconsin, Madison, Department of Geosciences, Madison, WI, United States

A B S T R A C T

The dome-and-keel granite-greenstone structures in the East Pilbara Terrane are commonly interpreted to result from a crustal overturn process that underpinned the growth and stabilization of continental crust on early Earth. We investigate the timing and timescales of this overturn process using integration of garnet and zircon geochronology with microstructural analyses. We use this integrated approach to provide insight into the evolution of dome-and-keel structures in the East Pilbara Terrane. Garnet Lu-Hf and Sm-Nd geochronology shows that two discrete periods of fabric development related to dome formation occurred between ~ 3.42 to 3.39 Ga and 3.34 to 3.30 Ga. The older population of garnet is mechanically disaggregated, and we interpret that their growth is related to an early metamorphic event in the East Pilbara that occurred prior to the main phase of dome-and-keel formation. The younger population of garnet, between 3.34 and 3.30 Ga, include garnet with post-kinematic growth structures. By coupling these microstructures and garnet Lu-Hf ages, we show that the main phase of dome formation is dated by this younger event of garnet growth at about 3.34 and 3.30 Ga. The Sm-Nd ages of these garnets are systemically younger than the Lu-Hf ages, consistent with protracted cooling of the system after dome formation. Together, these data show that dome-and-keel structures in the East Pilbara formed quickly, perhaps in a few tens of million years.

1. Introduction

Archean crustal blocks are distinct from younger Proterozoic and Phanerozoic terranes. Geochemically, Archean crust has less evolved bulk compositions, largely made up of tonalite-trondhjemite-granodiorite (TTG) complexes and mafic-to-ultramafic volcanosedimentary greenstone belts (Jahn et al., 1981). In most Archean Cratons, these lithologies are arranged in alternating granite-greenstone belts, where low-grade metavolcanic greenstones are juxtaposed directly next to high-grade TTG-gneiss terranes. These granite-greenstone assemblages are a hallmark of Archean crust (e.g., Jahn, et al., 1981; Condie, 1981; Hickman, 1984). Some granite-greenstone terranes have a distinct "dome-and-keel" architecture, where large (~70 km) ovoid TTG batholiths are separated by curvilinear greenstone belts. Dome-and-keel structures are found in Archean cratons around the world—notably the Kaapvaal (e.g., de Wit et al., 1992), Dharwar (e.g., Prabhakar and Bhattacharya, 2013), and Pilbara (e.g., Collins et al., 1998) Cratons. Of these, the dome-and-keel structures of the Pilbara and Kaapvaal cratons are the best preserved and exposed, and therefore have been the focus of intense study and debate about their significance for the evolution of early continental crust.

Archean dome-and-keel structures are often attributed to lithosphere-scale Rayleigh-Taylor instabilities (e.g., Sharp, 1984). This process involves buoyancy forces driving crustal overturn, causing dense mafic greenstones to sink into the middle and lower crust, while less dense granitic rocks are exhumed near the surface (Mareschal and West, 1980; Collins et al., 1998; Sandiford et al., 2004; Van Kranendonk et al., 2004). Collins et al. (1998) summarized this process in their "partial convective overturn" model, and presented it as the mechanism underlying the formation of dome-and-keel structures in the Pilbara Craton. Decades of research indicate that these structures are the cumulative products of several igneous, metamorphic, and deformational events, possibly related with multiple episodes of crustal overturn throughout the early Archean (see review by Hickman, 2021). However, the precise timescales and ages of these events remain to be fully understood.

The study of Archean crustal overturn events is significant as they may be responsible for creating preservable felsic crust on the early Earth before the onset of plate-style tectonics (Van Kranendonk et al., 2007). Therefore, determining age constraints on this process provides insight into how volumes of Archean crust evolved over time (e.g., Fyfe, 1978; Armstrong, 1981; Patchett and Arndt, 1986; Condie and Aster, 2010). The extraction of preservable felsic crust has major implications for the geochemical evolution of the depleted mantle reservoir

* Corresponding author.
E-mail address: salerno@wsu.edu (R. Salerno).

https://doi.org/10.1016/j.precamres.2023.107108
Received 19 January 2023; Received in revised form 25 May 2023; Accepted 26 May 2023
Available online 23 June 2023

(DePaolo, 1981; Hofmann, 1988).

Garnet geochronology is a valuable tool for deciphering the histories of deformed and metamorphosed rocks. Garnet can be dated using both the Lu-Hf (e.g., Duchêne et al., 1997; Blichert-Toft et al., 1999) and Sm-Nd (e.g., van Breemen and Hawkesworth, 1980; Mezger et al., 1992) isotope systems. Additionally, major and trace element (Spear, 1993; Spear and Kohn, 1996) compositional zoning patterns in garnet are helpful in interpreting isotopic ages as either the time of initial growth or of later re-equilibration. Additionally, garnet in deformed metamorphic rocks provides a wealth of microstructural information, as garnet incorporates matrix minerals during growth, thus "freezing in" rock fabrics (Spry 1969; Yardley et al., 1990) and can develop as porphyroblasts during deformation, both of which add important structural context to isotopic ages.

Despite the advantages of integrating garnet geochronology and microstructural analyses, this approach has yet to be applied to understanding the evolution of dome-and-keel structures in the Pilbara Craton due to an extremely limited number of garnet-bearing rocks found so far (see recent compilation by Hickman, 2021). The scarcity of garnet may be due to the overall low metamorphic grade of most supracrustal rocks in the area (Williams and Bagas, 2007) or may be related to protoliths with Al-, Fe-, Mn- or Mg-poor bulk compositions which cannot sustain garnet growth (e.g., Spear 1993).

This paper presents an approach that integrates garnet geochronology and microstructural analyses to understand crustal evolution on early Earth. To better understand the timing and timescales associated with early Archean crustal overturn, we focus on the metamorphic and deformational history of Paleoarchean dome-and-keel structures in the Pilbara Craton. We analyze seven newly found garnet-bearing samples in the Warrawoona Syncline–a belt of deformed supracrustal rocks between the Mt. Edgar and Corunna Downs Granitic Complexes–using garnet Lu-Hf and Sm-Nd geochronology, zircon U-Pb geochronology and Hf isotopes, and microstructural analysis. We demonstrate that most of these rocks have igneous protoliths which erupted between 3.46 and 3.44 Ga with chondritic initial Hf isotope compositions ($\varepsilon_{Hf(i)} \approx 0$). Garnet geochronology demonstrates that metamorphism in some samples reached garnet stability by 3.42 Ga, about ~ 30 Ma after protolith eruption. We document a second period of garnet growth between 3.34 and 3.29 Ga. The garnet with older ages record pre-kinematic growth structures, while the younger group includes garnet with post-kinematic growth structures. The microstructures of the younger garnet age group indicate that fabric development in the Warrawoona syncline ended between 3.34 and 3.29 Ga following a major dome-forming event. Our results contribute to the growing consensus that multiple punctuated crustal overturn events throughout the Paleoarchean played an important role in making early continental crust. Further, our Hf isotope data reinforces the model that Paleoarchean crustal overturn processes are closely related to the production of preservable felsic crust.

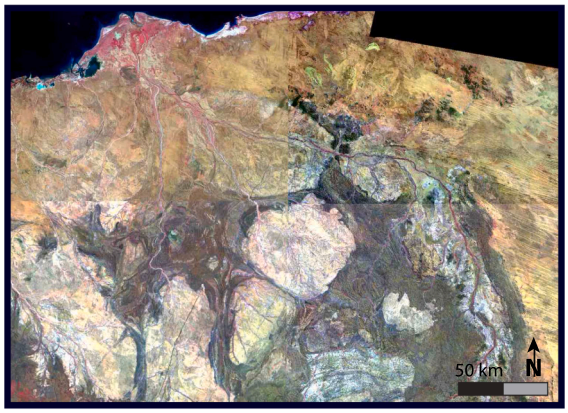

Fig. 1. Landsat image of the Pilbara Craton where the TTG domes are visible as light ovals and the greenstone keels appear as and darker belts. Image courtesy of Geoscience Australia.

2. Background

2.1. Geologic background of the East Pilbara Terrane

The Pilbara Craton, located in northwestern Australia, is divided into three main elements: the East Pilbara Terrane (3.59–3.22 Ga); the West Pilbara Superterrane (3.28–3.07 Ga); and the De Grey Superbasin (3.05–2.93 Ga), which unconformably overlie the older basement components (Van Kranendonk et al., 2006; Hickman, 2012). Of these, the East Pilbara Terrane contains the most ancient crustal material and Paleoarchean dome-and-keel structures. The two components that make up these dome-and-keel structures are metavolcanic and metasedimentary successions of the Pilbara Supergroup (forming the greenstone keels) and granitic complexes (forming the domes) (Fig. 1).

The Pilbara Supergroup is largely composed of basaltic and volcanoclastic rocks erupted between 3.53 and 3.23 Ga (e.g., Van Kranendonk et al., 2002; Smithies et al., 2005, 2007). The stratigraphy of the Pilbara supergroup itself is subdivided into four groups: the Warrawoona, Kelly, Sulfur Springs, and the Soanesville Groups (Van Kranendonk et al., 2007; Hickman, 2012). Each of these stratigraphic groups are separated by angular erosional unconformities which represent periods of uplift and deformation (e.g., Van Kranendonk et al., 2006). The metamorphic grade of these rocks ranges from greenschist to amphibolite facies, with higher grade more proximal to the margins of the granitic domes (e.g., Collins and Van Kranendonk, 1999). There are rare examples where the supracrustal rocks are enveloped into the granitic domes as metamorphic screens (e.g., François et al., 2014).

2.1.1. Supracrustal rocks in the Warrawoona Syncline

The Warrawoona Syncline is the northwest-trending part of the Marble Bar greenstone belt that occupies a narrow, attenuated zone between the Mt. Edgar Granitic Complex to the north and the Corunna Downs Granitic Complex to the south. The southwestern limb of the Warrawoona Syncline is dominated by Kelly Group rocks. The northeastern limb, which is the focus of this study, is comprised of Warrawoona Group rocks. The peak metamorphic mineral assemblages in the Warrawoona Group here include kyanite and garnet (Collins and Van Kranendonk, 1999). The blocks of supracrustal material enveloped inside the Mt. Edgar Granitic Complex have garnet-sillimanite peak metamorphic mineral assemblages consistent with amphibolite to granulate facies conditions (François et al., 2014). Chlorite is present in all these rocks, which may be related to either retrograde metamorphism or later greenschist facies overprinting in the Neoarchean (Collins et al., 1998; Zegers et al., 1998; Roberts et al., 2022).

2.1.2. Granitic rocks

The Mt. Edgar Granitic Complex (MEGC) adjacent to the Warrawoona Syncline, and all other dome complexes in the Pilbara Craton, are composed of multiple generations of granitic rocks which crystalized between 3.60 and 2.82 Ga (Van Kranendonk et al., 2007). These multiple generations of magmatism have been divided into five granitic supersuites based on U-Pb zircon ages. These are the Callina (3484–3462 Ma), Tambina (3451–3416 Ma), Emu Pool (3324–3290 Ma), Cleland (3274–3223 Ma), and the Split Rock (2851–2831 Ma) supersuites (Van Kranendonk et al., 2007; Champion and Smithies, 2007 Hickman, 2012). The four oldest supersuites are related to the formation of the dome-and-keel structures, while the youngest supersuite (Split Rock) is largely thought to be post-tectonic (Sweetapple and Collins, 2002; Van Kranendonk., 2002; 2007). The Callina and Tambina rocks are generally preserved near the margins of the domes, where they are deformed into gneisses (Williams and Collins 1990; Williams and Bagas, 2007). The Emu Pool and Cleland rocks constitute a larger volumetric component of the granitic rocks in the East Pilbara, and include

intrusions with more evolved bulk compositions (e.g., higher Na and K content; Mackey and Richardson, 1997).

2.2. Timing of dome-and-keel formation in the East Pilbara Terrane

Numerous studies have been dedicated to documenting the deformational and tectonic history of the dome-and-keel structures in the East Pilbara Terrane. Hickman (1983, 1984), Collins (1989), and Williams and Collins (1990) interpreted that the Pilbara dome-and-keel pattern formed by vertical-style tectonics. The resulting models proposed that solid-state granite diapirism was primarily responsible for driving dome-forming processes. Collins et al. (1998) later suggested a multi-stage process involving "partial convective overturn" of the upper to middle crust. In their model, a TTG sheet and sill complex first intruded an older supracrustal greenstone succession. This intrusion was followed by eruption of basaltic layers, burying the older succession and TTG complex to mid-crustal depths and creating an inverted crustal density gradient. As a result, the buried older rocks were heated, weakened, and partially melted, allowing the crust to reorganize through partial convective overturn, where the denser greenstones sank and accommodated exhumation of the more buoyant granitic rocks (Van Kranendonk et al., 2004; Sandiford et al., 2004; Thèbaud and Rey, 2013; François et al., 2014; Wiemer et al., 2018). The presence of kyanite-bearing metamorphic assemblages inside the Warrawoona Syncline is used to argue that partial convective overturn was a crustal-scale process, where supracrustal rocks were buried to depths exceeding 20 km (Collins et al., 1998; Collins and Van Kranendonk 1999).

Van Kranendonk et al. (2004, 2007) constrained doming events through time using relationships between deformed rocks and dated igneous intrusions. Early (i.e. pre 3.40 Ga) deformation has been documented by multiple authors (Collins 1989; Nelson 1999; Van Kranendonk et al., 2004; Hickman 2021). Van Kranendonk et al. (2004, 2007) argue that the main amplitude of the dome-and-keel architecture in the Pilbara Craton likely formed between 3.33 and 3.31 Ga. Wiemer et al. (2018) integrated igneous, metamorphic, and detrital U-Pb geochronology to argue that the Pilbara dome-and-keel structures formed through three separate overturn events, starting at ~ 3.48 Ga. Further, they hypothesized that these events operated on ~ 100m.y. cycles.

This main period of dome formation was synchronous with the emplacement of the Emu Pool Supersuite and the development of several shear zones along the margins between domes and greenstone belts (e.g., Williams and Collins 1990; Collins et al., 1998; Collins and Van Kranendonk, 1999; Pawley et al., 2004). Several thermotectonic events followed the primary formation of the dome-and-keel structures in the Pilbara Craton, including: (1) intrusion of the Split Rock and Sisters Supersuites in the Neoarchean and; (2) deposition of the overlying Fortescue group, which Van Kranendonk et al. (2006) argues "reamplified" the dome and-keel structures.

3. Methods

The analytical methods used for garnet Lu-Hf and Sm-Nd isotope dilution analyses (Anczkiewicz and Thirwall, 2003; Goodge and Vervoort, 2006; Cheng et al., 2008; Johnson et al., 2018), and for laser ablation split stream zircon U-Pb and Hf isotope analyses (Fisher et al., 2011, 2014; Fisher and Vervoort, 2018), have been described elsewhere, and are also detailed in Appendix 1. The analytical methods for garnet major and trace element analyses are also described in Appendix 1. The U-Pb and Hf isotope values of secondary mineral standards used in this study are reported in Appendix 2.

4. Results

4.1. Sample mineralogy and bulk compositions

Seven samples were collected from the Warrawoona Group along strike of the Warrawoona syncline (Table 1; Fig. 2). One additional sample, AME18-138, was collected from an enclave of metamorphosed supracrustal rocks inside the Mt. Edgar Granitic Complex. Detailed petrographic descriptions are reported in the Appendix 3.

Most of these samples have a matrix mineralogy rich in quartz and feldspar. The foliation fabric in the matrix of most rocks is defined by chlorite, which seems to be replacing biotite. In addition to chlorite, there are also examples where foliation and lineation are defined by amphibole (AME18-058), muscovite (AME18-060, AME18-078), and sillimanite (AME18-138). Sample AME18-138 is the only sample where sillimanite is part of the peak metamorphic mineral assemblage. All samples contain garnet except for AME18-078. Epidote is a common minor mineral phase in the matrix of most of these samples. Chloritoid is also a minor phase, but is only seen in AME18-060. Sample AME18-031 is unlike most of these rocks, with a higher abundance of amphibole and chlorite in the matrix and significantly less quartz and feldspar.

Garnet porphyroblasts range in size between 1 mm and 1.2 cm. Most garnets are inclusion-rich, fractured, and have anhedral shapes. In some cases, these fractures are filled with chlorite, which is likely forming at the expense of garnet (e.g., AME18-028, AME18-060).

The quartzofeldspathic mineralogy of most of these samples corresponds with bulk rock compositions high in silica (67–78 wt%). On a total alkali vs. silica diagram (Appendix 4), these correspond with dacite and rhyolite protolith compositions. One sample (AME18-031) is silica-poor (~52 wt%) and has higher concentrations of Fe and Mg (>12 wt%), corresponding to a more basaltic protolith composition. The concentrations of fluid mobile elements (i.e., Nb, Rb, Ca) varies between these samples. Most have high Na_2O/K_2O (2–9) and low Al_2O_3/Na_2O (3–9) ratios, which are typical values for igneous rocks (White and Chappell, 1983). AME18-028 and AME18-138, however, have much higher Al_2O_3/Na_2O ratios (>70), and lower Ca (CaO 0.2–0.9 wt%) and Na ($Na_2O \lesssim$ 0.1 wt%) relative to the other samples. Most samples have typical low bulk rock Rb/Sr ratios (<0.5), except for AME18-138 which is as high as 6.

4.2. Zircon U-Pb and Hf isotopes

Six of the eight samples in this study yielded zircon. For the zircon-bearing samples, zircon was separated and analyzed for U-Pb ages and Lu-Hf isotopes by laser ablation split stream (LASS)-MC-ICPMS. The zircon U-Pb isotope compositions are plotted on concordia diagrams in Fig. 3. Back-scattered electron images (BSE) of representative zircons from each sample are shown in Appendix 4. The zircon LASS-MC-ICPMS U-Pb and Hf isotope data for standards and unknowns are reported in the Appendix 1 and 2.

Between these six samples, zircon grains range in size between 60 μm and 500 μm (long axis). Some zircon are euhedral and have well-formed terminations, (e.g., grain #18 in sample AME18-060 of Appendix 4). In plain light, most zircon are translucent with a brown-green hue and waxy luster. These features are typical for very old zircon which have some degree of radiation damage. These BSE images show that all zircon have oscillatory zoning patterns with no evidence for later overgrowths.

The U-Pb data in each sample show some degree of discordance related to Pb-loss, which is as great as 20% (in the case of AME18-078). Some samples have reversely discordant analyses that plot above concordia. The U-Pb data from all samples form well-defined discordia lines with present-day lower intercepts and upper intercept ages between 3.46 and 3.44 Ga (Fig. 3). The intercept age of each sample agrees well with the corresponding mean $^{207}Pb/^{206}Pb$ age of these analyses, consistent with present-day Pb-loss. The Th/U ratios of all zircon range between 0.2 and 1.4, with a few as high as ~ 4.0 (Appendix 4).

Table 1
A summary of the name, location, lithology, and geochronology for the 8 samples in this study. Coordinates are given in decimal degrees.

Sample	Lat/Long	Lithology	Zircon U-Pb age (2SE)	Mean zircon ε_{Hf}(i) (2SE)	Garnet Lu-Hf age (2SE)	Garnet Sm-Nd age (2SE)
AME18-028	−21.418060, 120.177025	Garnet schist	3445 ± 36	+0.6 ± 0.7	3418 ± 28	3173 ± 14
AME18-031	−21.418652, 120.176600	Amphibole-garnet schist	–	–	3321 ± 17	–
AME18-053	−21.368114, 119.967945	Garnet schist	3455 ± 35	+0.2 ± 0.3	3337 ± 11	3317 ± 27
AME18-058	−21.350842, 119.945076	Amphibole-muscovite-garnet schist	3461 ± 21	+0.8 ± 0.3	3298 ± 35	3252 ± 15
AME18-060	−21.348535, 119.945929	Muscovite-chloritoid-garnet schist	3440 ± 35	+0.2 ± 0.2	3411 ± 53	3358 ± 13
AME18-078	−21.326597, 119.902234	Muscovite schist	3447 ± 35	+0.6 ± 0.2	–	–
AME18-080	−21.386794, 119.995261	Garnet schist	3452 ± 40	+0.4 ± 0.1	–	3283 ± 39
AME18-138	−21.327168, 120.173576	Biotite-sillimanite-garnet schist	–	–	3390 ± 37	3307 ± 14

The corresponding zircon Lu-Hf isotope data have characteristically low $^{176}Lu/^{177}Hf$ values (0.0005 to 0.0053) and a narrow range of initial $^{176}Hf/^{177}Hf$ values. Figure 4 shows the initial $^{176}Hf/^{177}Hf$ values of zircon in each sample, determined at the sample's interpreted crystallization age. The Hf isotope compositions of these zircon are remarkably consistent, both within each sample and between samples. The mean $^{176}Hf/^{177}Hf$ values range from 0.280553 ± 8 to 0.280569 ± 6, corresponding to broadly chondritic $\varepsilon_{Hf(i)}$ values between + 0.2 ± 0.3 and + 0.8 ± 0.3.

4.3. Garnet chemistry and zonation

Major element line-transects and compositional maps of select garnet grains were made by electron microprobe (EPMA) (Fig. 5). The garnet in all samples are generally almandine-rich (Alm_{54-83}) with lower and variable amounts of spessartine, grossular, and pyrope ($Sp_{3-20}Gr_{3-19}Py_{2-14}$). Sample AME18-080 has the highest grossular content ($Gr_{\sim 18}$) compared to the other samples. The pyrope content also varies between these samples, as some samples have lower Mg concentrations (Py_{2-6}; e.g., AME18-053), while others have higher concentrations (Py_{9-13}; e.g, AME18-138). Most samples are zoned in manganese content, where core domains are more spessartine rich (Fig. 5). The opposite is true about the behavior of almandine and pyrope content, which covary and are depleted in the core domain relative to the rim.

Trace element line scans were conducted by LA-ICPMS; across the same line transects measured for major elements by EPMA; the Sm and Lu concentrations for these transects are shown Fig. 5. Samarium shows no significant variation across the transects, while Lu is higher in the core of AME18-031 and AME18-138 and is elevated toward the rim in AME18-080 and AME18-060. Concentrations of Lu and Sm are generally below 1 ppm in the garnet.

4.4. Microstructures

The internal structures of garnet and their relationship with the surrounding matrix were evaluated for all seven garnet-bearing samples. Representative images of garnet and textures in these samples are shown in Fig. 6. The Warrawoona Syncline samples have well-formed foliations which are parallel with the dominant foliation of the Warawoona Syncline (D4 of Collins 1989), which is parallel with the margin between the syncline and neighboring MEGC (see stereonets in Fig. 2). These samples also have have steeply plunging lineations. In thin section, foliation is defined by chlorite (Fig. 6A), amphibole (Fig. 6C and E), and muscovite (Fig. 6F). Garnet varies from euhedral (Fig. 6 C) to anhedral (Fig. 6F and I). Some garnet have disaggregated microstructures, which is when larger porphyroblasts appear to be mechanically broken into smaller fragments and the pieces are sheared into disseminated masses parallel to the dominant foliation (Fig. 6B and F, Appendix 4). In nearly every case, except for AME18-031, the dominant foliation is deflected and curved around the larger garnet grains.

The garnet contain inclusions of quartz, ilmenite, and minor plagioclase. In AME18-138, sillimanite is both an inclusion and matrix phase. In several samples, quartz inclusions are arranged in bands, which appear to represent an earlier foliation fabric overgrown by garnet. Some garnet also contain ilmenite inclusions, which are also parallel to these quartz bands (e.g., AME18-058).

A summary of key microstructural relationships observed in the garnet-bearing samples is given in Fig. 7 where we highlight three important observations. First, garnet deflects the foliation in all samples except AME18-031 (Fig. 7A and B). This deflection is recorded both by the bending of foliation-defining mineral bands and in some cases the attenuation in the regular spacing of fabric at the point of maximum curvature (as in Fig. 7B). By contrast, foliation continues through garnets uninterrupted in sample AME18-031 (Fig. 7C and Appendix 4). Second, garnet that deflect the foliation vary in their shape and internal structure. Garnet in sample AME18-053 are subhedral and have ilmenite inclusions with a shape preferred orientation that is subparallel to ilmenite needles in the matrix (Fig. 7A). In contrast, garnet in sample AME18-058 is asymmetrically sigmoidal in shape and has co-parallel quartz inclusion bands and ilmenite inclusions that progressively rotate from the core to the rim of the garnet, with orientation of rim inclusions most closely matching the matrix foliation (Fig. 7B). Third, garnet in sample AME18-031 – the only example where foliation is not deflected around garnet – are by far the most euhedral garnet of any sample, with straight crystal boundaries and angular corners.

4.5. Garnet geochronology

Seven of the eight samples in this study contain garnet; AME18-078 does not. Of these, we determined both garnet Lu-Hf and Sm-Nd ages for 5 samples. The Sm-Nd data for sample AME18-031 are not plotted as these analyses did not yield a valid isochron. The Lu-Hf geochronology for sample AME18-080 was also not successful. A summary of whole rock and garnet Lu-Hf and Sm-Nd isotope data, as well as Lu, Hf, Sm, and Nd concentrations, is presented in Table 2. The Lu-Hf and Sm-Nd isochrons are plotted in Figs. 8 and 9.

Garnet in these samples have Lu concentrations between 1.4 and 5.5 ppm and Hf concentrations between 0.9 and 5.0 ppm. These values correspond to garnet $^{176}Lu/^{177}Hf$ between 0.0521 and 0.7614 and $^{176}Hf/^{177}Hf$ values between 0.283973 and 0.329454. The whole rock aliquots have lower $^{176}Lu/^{177}Hf$, between 0.0110 and 0.0344, and correspondingly less radiogenic $^{176}Hf/^{177}Hf$, between 0.281266 and

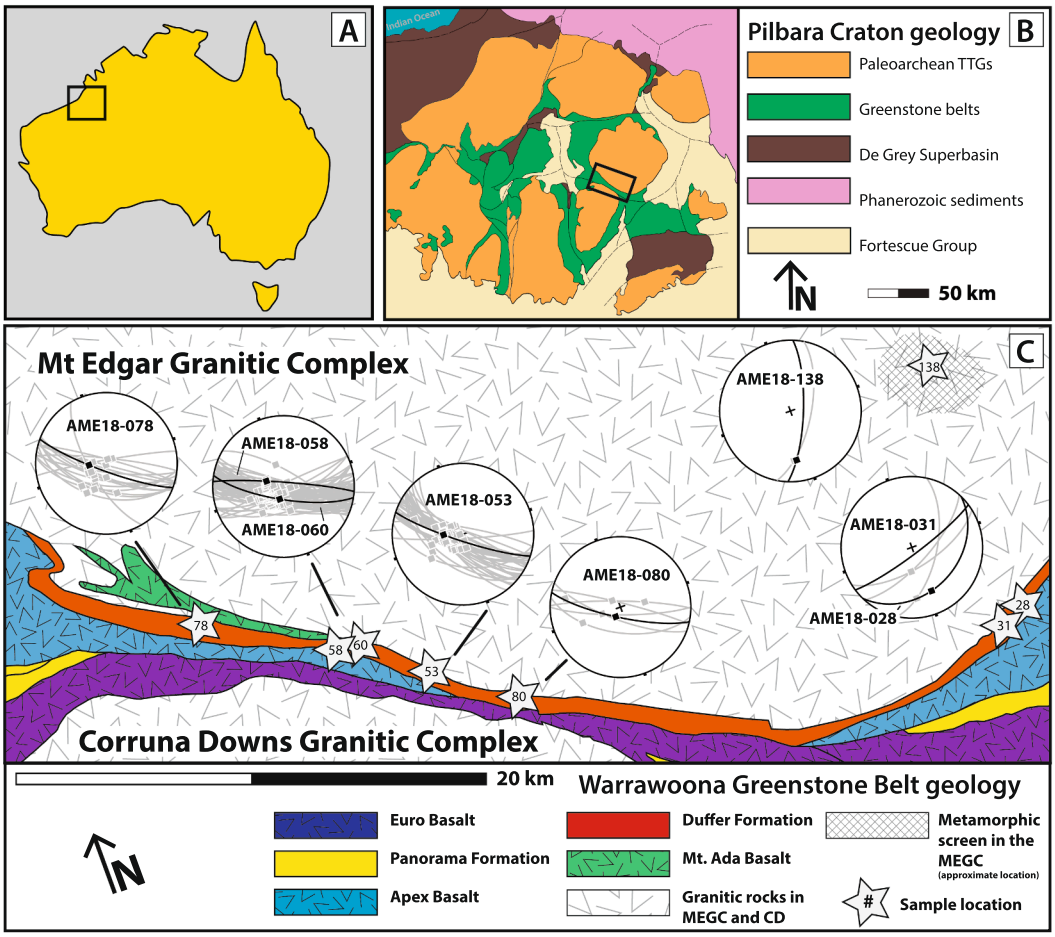

Fig. 2. A. The location of the Pilbara Craton in Australia. B. Simplified map of the regional geology of the Pilbara Craton. The box indicates the location of the Warrawoona syncline Belt. C. Generalized geology and sample locations in the Warrawoona Syncline in the study area. Geology after Hickman (2012). The equal area nets on panel C plot the dominant macroscopic foliation and lineation. Black measurements were collected at the sample location. Grey measurements were collected in the area surrounding each sample (<750 m). The foliation and lineation measurements were used when cutting oriented thin sections.

0.282852. Chloritoid was a mineral phase in sample AME18-060 and was analyzed as well, with a $^{176}Lu/^{177}Hf$ of 0.0257 and $^{176}Hf/^{177}Hf$ of 0.282318, near the whole rock values.

The Lu-Hf isotope data regress reasonably well-defined isochrons (MSWD values 0.5–4.9), with ages between 3298 ± 35 and 3418 ± 28 Ma. These isochrons have intercepts that correspond to initial ε_{Hf} between –2.1 and + 2.1. In every case, the $\varepsilon_{Hf(i)}$ values of the individual whole rock and mineral aliquots agree when determined at the isochron age, and these also agree with the intercept $\varepsilon_{Hf(i)}$ values (Table 2). The Lu-Hf ages of these 6 samples fall into two groups which are outside of 2SE uncertainty from one another. Samples AME18-138, AME18-060, and AME18-028 have ages which overlap within uncertainty, between 3418 ± 28 and 3390 ± 37 Ma. The younger group of Lu-Hf ages consists of AME18-058, AME18-053, and AME18-031, which also have ages overlapping within uncertainty, between 3337 ± 11 and 3298 ± 35 Ma (Fig. 10).

Samarium and neodymium isotopes were determined for the same garnet aliquots measured for Lu-Hf isotopes. Garnet aliquots have Sm concentrations between 1.3 and 4.4 ppm and markedly higher Nd concentrations between 3.1 and 13.6 ppm. These values correspond to $^{147}Sm/^{144}Nd$ ratios between 0.1266 and 0.2650 and $^{143}Nd/^{144}Nd$ between 0.512967 and 0.515900. The whole rock aliquots generally have higher Sm and Nd concentrations, between 1.4 and 5.6 ppm and 6.2–17.5 ppm, respectively. The whole rock $^{147}Sm/^{144}Nd$ ratios range from 0.1157 to 0.1828 and $^{143}Nd/^{144}Nd$ from 0.510745 to 0.512400.

The Nd concentrations of the dissolved garnet aliquots are much higher than the values typically expected for pure garnet – up to 13.6 ppm in some cases. Such high Nd concentrations may reflect incorporation of Nd-rich phosphate minerals (e.g., apatite and monazite) during garnet digestion. Incorporation of these phosphate minerals during garnet digestion may be problematic for Sm-Nd geochronology for several reasons (Scherer et al., 2000). The contribution of Nd from these minerals will lower $^{147}Sm/^{144}Nd$ and $^{143}Nd/^{144}Nd$ in the garnet aliquot. This will both bias the measured garnet $^{143}Nd/^{144}Nd$ value toward the Nd composition of the phosphates and lower the measured garnet $^{147}Sm/^{144}Nd$ and $^{143}Nd/^{144}Nd$, which reduces the "spread" of the isochron, thereby decreasing the precision of the age regression. A further concern is that phosphate minerals may be disturbed at lower temperatures, resulting in open-system Sm-Nd isotope behavior (e.g., Hämmerli et al., 2014). In this case, the isochron may not record the timing of initial closure of the Sm-Nd system in garnet.

To assess and minimize the effects of LREE-rich phosphate minerals, when possible, we analyzed two additional garnet aliquots that were treated with H_2SO_4 prior to final digestion following the method of Anczkiewicz and Thirlwall (2003). This step is designed to preferentially leach accessory phosphate minerals from the garnet prior to final digestion. Sulfuric acid leaching could not be done for sample AME18-080, and AME18-031 due to lack of material. In every case, H_2SO_4 leaching lowered the measured Nd concentration and increased the measured $^{147}Sm/^{144}Nd$ and $^{143}Nd/^{144}Nd$ the garnet aliquots (Table 2). For example, Nd concentrations of the leached garnet in AME18-028 are 0.75 ppm, which is much lower than the Nd content of the unleached

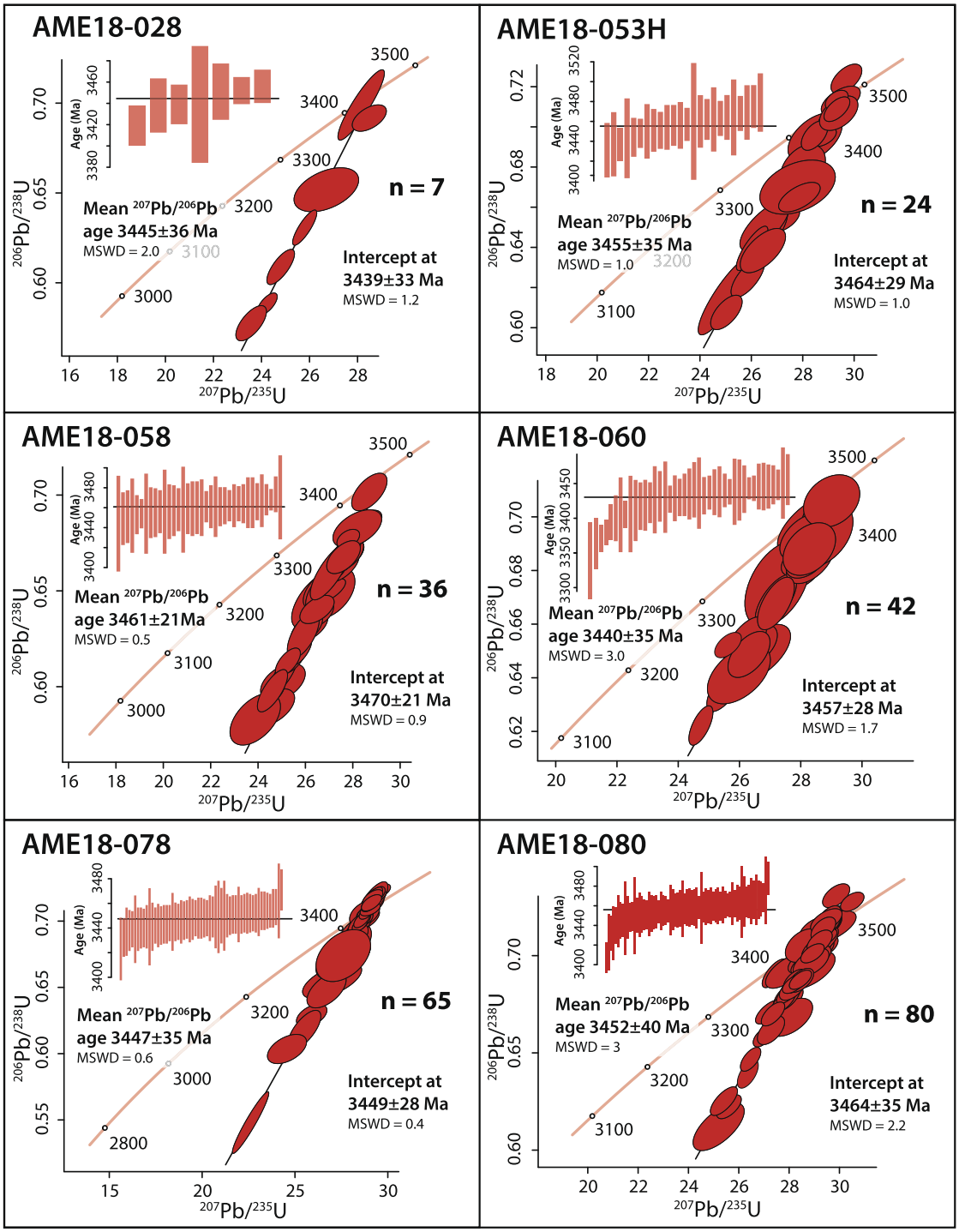

Fig. 3. Concordia plots of zircon LASS U-Pb data for six samples from the Warrawoona Syncline. The insets show the $^{207}Pb/^{206}Pb$ dates, and the associated weighted mean dates. All uncertainties are shown at 2SE.

aliquots of ~ 5.5. This is also the case for sample AME18-060, where the leached garnets have ~ 0.4 ppm Nd, much lower than the unleached garnets (up to 9 ppm Nd).

The regression of Sm-Nd isochron ages is less straight forward, as the garnet aliquots leached with H_2SO_4 have systematically higher $^{147}Sm/^{144}Nd$ and $^{143}Nd/^{144}Nd$ ratios than the unleached garnets. This results in two possible Sm-Nd regressions for each sample: one "leached age", determined with the whole rock and then leached garnet aliquots, and second "unleached age", calculated using the whole rock and unleached garnet aliquots. The leached ages range between 3358 ± 13 and 3173 ± 14 Ma and have low MSWD values and define 3 groups outside of uncertainty from one another (Figs. 9 and 10). Correspondingly, the unleached ages are generally younger and range between 3283 ± 39 and 2835 ± 68 Ma. In every case, the leached ages are systematically older, more precise, and are outside of 2SE precision from the unleached ages. Further, the $\varepsilon_{Nd(i)}$ values of the individual whole rock and sulfuric leached garnet aliquots agree when calculated at the leached Sm-Nd age. In contrast, the individual $\varepsilon_{Nd(i)}$ values of the

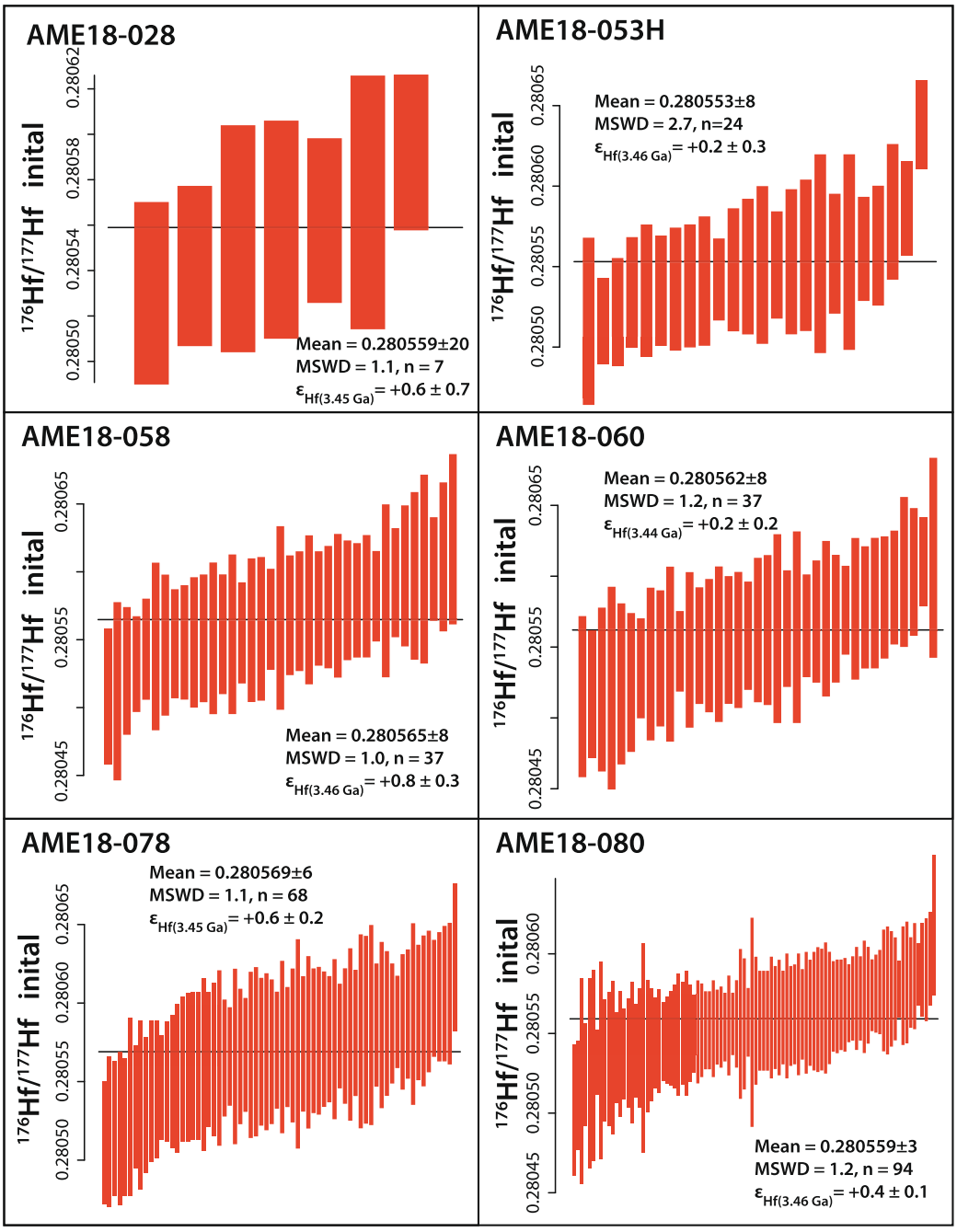

Fig. 4. The initial $^{176}Hf/^{177}Hf$ values of the zircon data plotted in Fig. 3, determined at each sample's respective mean $^{207}Pb/^{206}Pb$ age. All uncertainties are shown at 2SE. Initial values are calculated using the values of $^{176}Hf/^{177}Hf$ of $CHUR_{(0)} = 0.282785$ and $^{176}Lu/^{177}Hf$ of $CHUR_{(0)} = 0.0336$ (Bouvier et al., 2008), and with the ^{176}Lu decay constant of $1.867x10^{-11}$ yr^{-1} of Söderlund et al. (2004).

unleached aliquots are less radiogenic when calculated at the unleached age. These relationships suggest the material removed by sulfuric acid treatment was not in age and Sm-Nd isotopic equilibrium with garnet.

5. Discussion

5.1. Significance of zircon crystallization ages and Hf isotope compositions

In order to explore the significance of the zircon age and isotope data, it is important to consider the nature of the protoliths of these rocks. We argue that most samples have igneous protoliths, reflected by their high Na_2O/K_2O (2–9) and low Al_2O_3/Na_2O (3–9) (e.g., White and Chappell, 1983). Two samples have elevated Al_2O_3/Na_2O ratios suggesting some interaction with water, either during the sedimentary cycle or through hydrothermal alteration (McLennan et al., 1993). The latter case may be true for AME18-138, which has an elevated Rb/Sr ratio and high Al content, both of which are typical effects of hydrothermal alteration (Wickman et al., 1983). AME18-028 does not have a high Rb/Sr ratio, so it is possible that Na depletion of this rock relates to a sedimentary origin.

Overall, the bulk rock geochemical data indicate that the zircon bearing rocks, except for AME18-028, likely have igneous protoliths so we can make two important interpretations using the zircon U-Pb and Hf

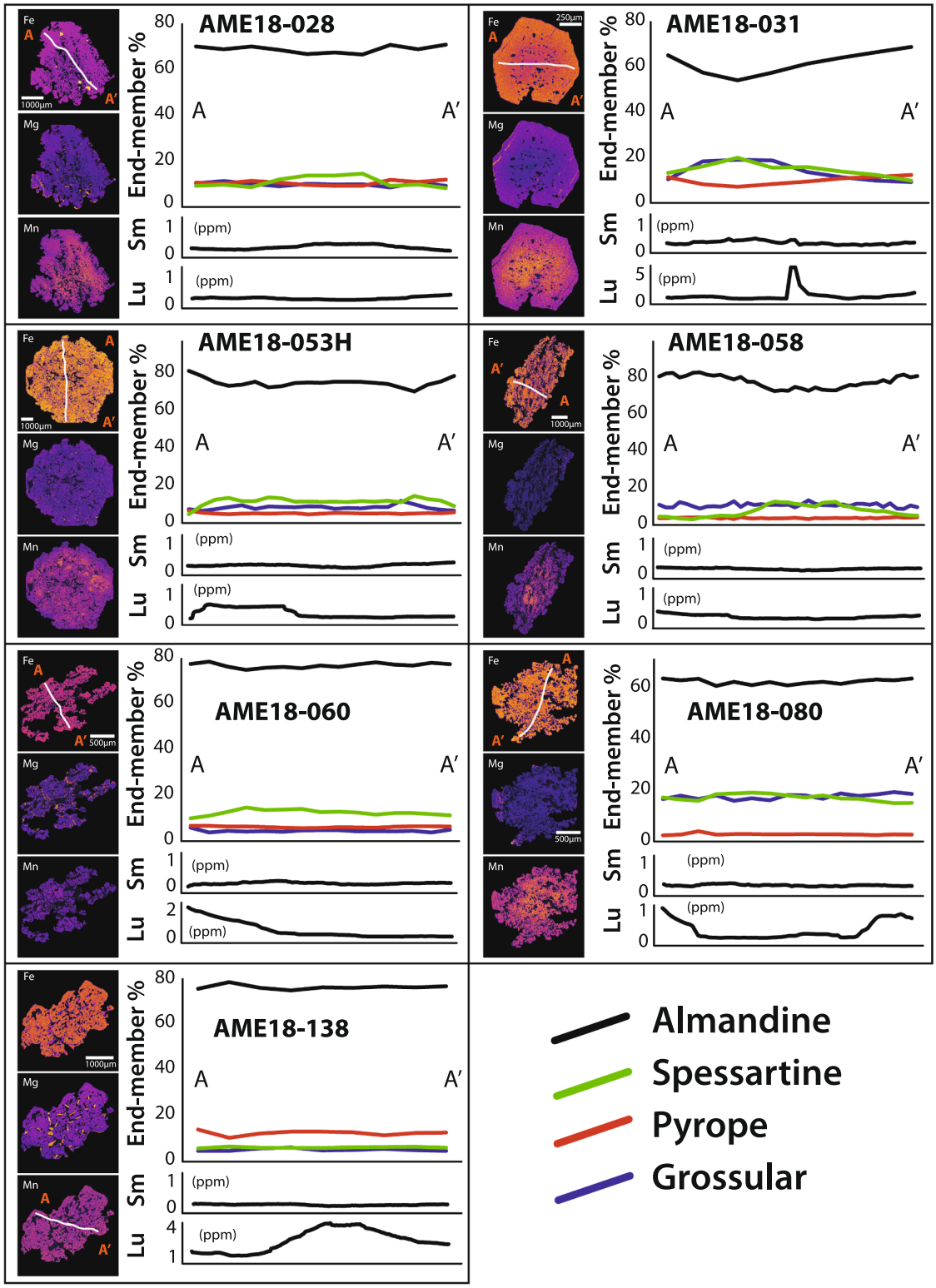

Fig. 5. Compositional maps of garnet showing relative Fe, Mg, and Mn compositions for the seven garnet-bearing samples in this study. The warmer colors correspond to relatively higher concentrations. The compositional profiles across the garnets show variations in end-member compositions as well as and Lu and Sm concentrations. The grey lines on the compositional maps between A and A' show the location of the major and trace element transects on each grain.

isotope data. First, the zircon U-Pb ages represent the igneous eruption/crystallization age of the protoliths, establishing the upper limit of the time interval between surface exposure and metamorphism. Second, igneous zircon record the initial Hf isotope compositions of protolith parent melts, and are useful for tracking the amount of inherited older crustal material into these rocks. Previous work has argued for the presence of older crust beneath the Pilbara Craton, using > 3.5 Ga detrital zircon grains and xenocrysts in the Pilbara supergroup as evidence (Thorpe et al., 1992, Van Kranendonk et al., 2007). Others have also interpreted the unradiogenic initial Sm-Nd isotopic compositions of

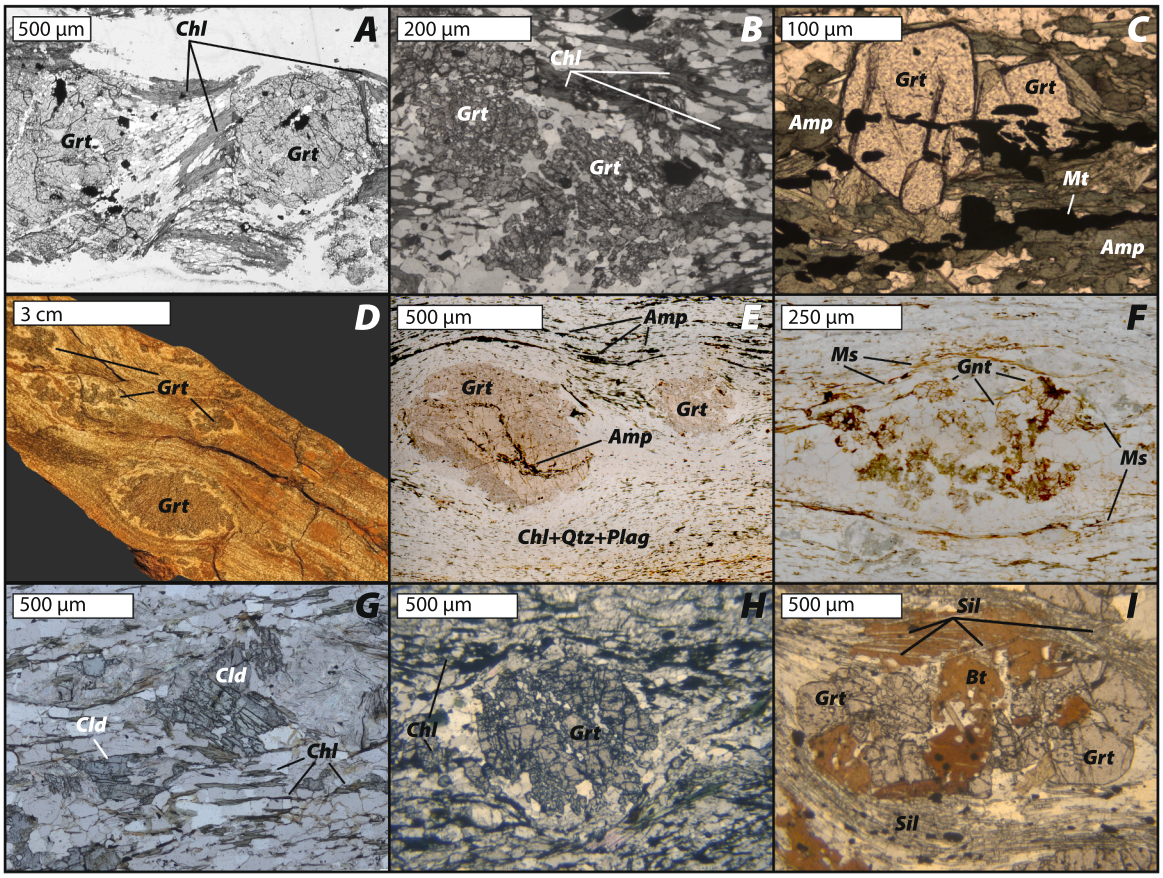

Fig. 6. Thin section and hand sample photographs of garnet and other minerals in samples from this study: A) Plane polarized light (PPL) image of garnet in AME18-028; B) PPL image of another garnet in AME18-028 with disaggregated microstructure; C) PPL image of euhedral garnet in AME18-031 which overgrows the foliation fabric; D) hand sample photo of garnet in AME18-053 showing garnet surrounded by quartzofeldspathic halos; E) PPL image of curved inclusion bands in garnet of sample AME18-058; F) PPL image of disaggregated garnet in sample AME18-060; G) PPL image of chloritoid in sample AME18-060; H) PPL image of garnet in sample AME18-080; and I) PPL image of garnet in sample AME18-138.

both granitic (Gruau et al., 1987; Bickle et al., 1993) and volcanic rocks (Tessalina et al., 2010) as evidence that the melt source of these rocks had a long crustal residence time, up to 4.3 Ga (e.g., Tessalina et al., 2010). Our data, rather, do not reflect any significant assimilation of Eoarchean or Hadean crust, consistent with recent isotope studies in the Pilbara Craton (Petersson et al., 2019, 2020; Murphy et al., 2021; Tympel et al., 2021; Salerno et al., 2021; Kemp et al., 2023). From this point of view, the chondritic $\varepsilon_{Hf(i)}$ values we report reflect overwhelmingly juvenile magmatism, without significant reworking of older crust. Our data thus provide no evidence for an older crustal basement beneath the Pilbara Craton, and further imply a relationship between crustal overturn events and juvenile magmatism.

5.2. Garnet compositions and growth patterns

Garnet in most samples have core domains enriched in Mn (e.g., AME18-031). These zoning patterns are typically attributed to metamorphic garnet growth and Rayleigh fractionation of major elements (Otamendi et al., 2002). Sample AME18-138, however, has relatively little variation in major element composition that might suggest major element zoning was thermally relaxed after initial garnet growth (e.g., Caddick et al., 2010). This result is consistent with the presence of stable sillimanite in AME18-138, which suggests this sample experienced higher-grade metamorphic conditions relative to the other samples in this study.

Most garnet in these samples show little variation in Sm and Lu concentration along the profiles in Fig. 5. However, some samples do show compositional zoning in Lu. Samples AME18-031 and AME18-138 both have "bell-shaped" Lu profiles which are commonly associated with primary growth zoning. This pattern reflects Rayleigh fractionation of HREE during initial garnet growth, in which Lu is strongly partitioned into the core (e.g., Hermann and Rubatto, 2003; Rubatto et al., 2020). Sample AME18-060 has an asymmetrical Lu profile, which may indicate the analyzed grain was not perfectly sectioned through the middle. Sample AME18-080 has reverse Lu zonation, where concentrations are relatively higher in the rims. A Lu-Hf age could not be determined for AME18-080, so it is difficult to interpret the significance of the Lu zoning in this sample.

5.3. Interpreting the timing of garnet growth

A major focus of this study is to determine the timing of garnet growth, to help provide timing constraints on the microstructures in these samples, and ultimately help constrain the timing of dome formation. However, garnet Lu-Hf and Sm-Nd ages can represent either: (1) the timing of garnet growth; or (2) the time elapsed since conditions in the system dropped below the Lu-Hf and/or Sm-Nd closure temperatures. Therefore, it is important to distinguish between these two scenarios.

Our garnet dates can be used to estimate the timing of garnet growth in these samples, as there is no evidence that metamorphic temperatures exceeded the closure temperature of either the Lu-Hf and Sm-Nd systems in garnet (Scherer et al., 2000; Smit et al., 2013). Therefore, we expect the Lu-Hf and Sm-Nd ages to agree and both record the timing of initial

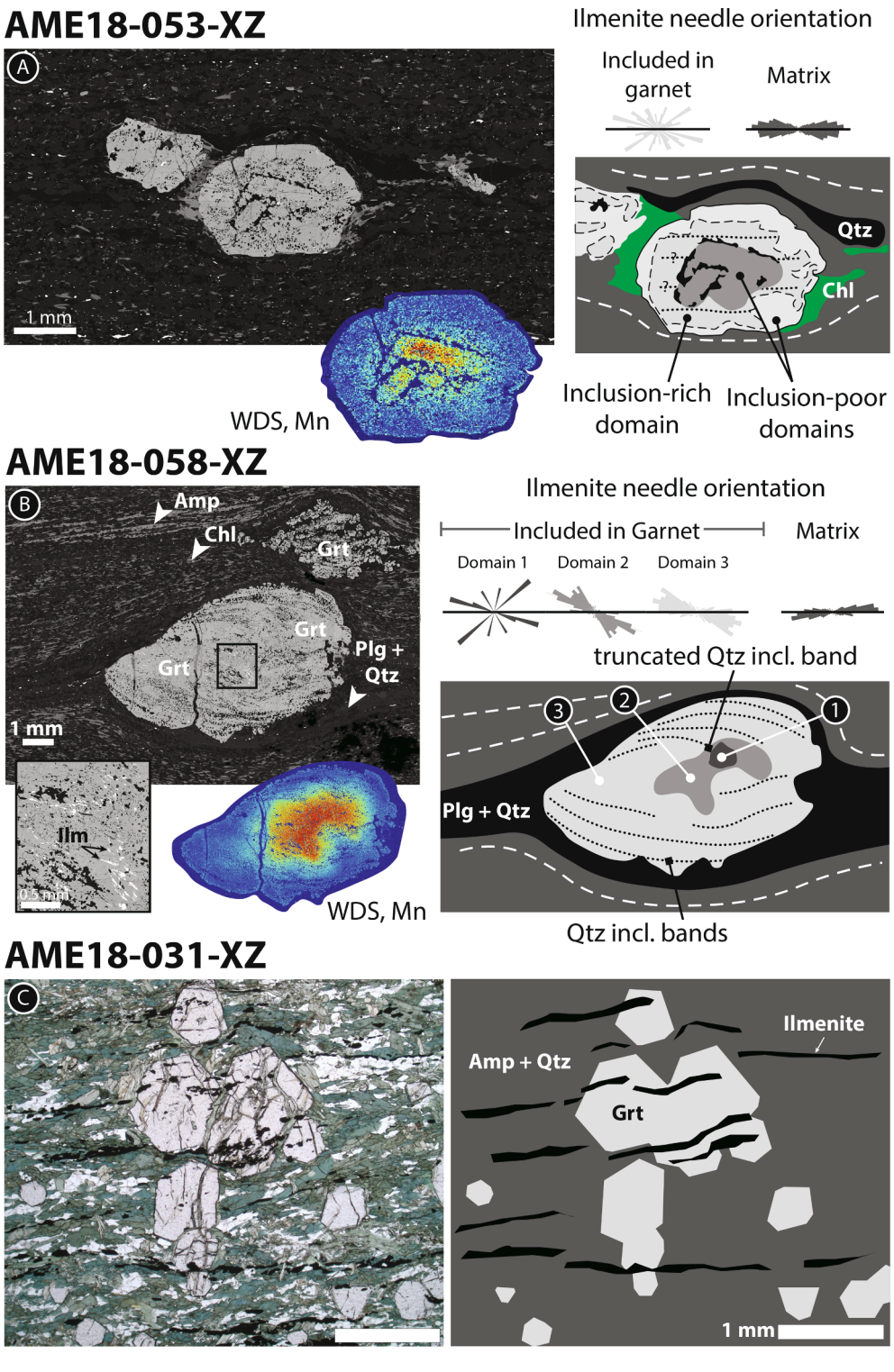

Fig. 7. Microstructural analysis of three samples from the Warrawoona Syncline. A) Sample AME18-053. The left panel is a BSE image with a Mn X-ray map inset. The right panel is a schematic illustration of major features. Rose diagrams show the orientations of ilmenite grains included in garnet and the matrix. B) Sample AME18-058. Left panel is a BSE image with two insets: a close up to show well aligned ilmenite inclusions in garnet and an Mn X-ray map. The right panel is a schematic illustration of major features. The rose diagrams show the orientations of ilmenite grains included in garnet and the matrix. C) Sample AME18-031. The left panel is a plane polarized light image. The right panel is a schematic illustration of major features.

garnet growth. This is the case for samples AME18-053, AME18-058, and AME18-060, where the Lu-Hf and Sm-Nd ages agree within uncertainty (Fig. 10).

This agreement, however, is not the case in samples AME18-138 and AME18-028, where the sulfuric acid treated Sm-Nd ages are younger than the Lu-Hf ages, outside of precision. As opposed to all other samples in this study, AME18-138 has stable sillimanite in its mineral assemblage, as well as melt stringers and pockets of leucosome at outcrop, indicating temperatures exceeded ~ 550° C (Appendix 4). It is also important to note this sample was collected from a block of greenstone material that was enveloped in Emu Pool age granitic rocks within the Mt. Edgar Granitic Complex. Previous thermodynamic modeling by François et al. (2014) indicates that P-T conditions at this outcrop exceeded the middle-amphibolite facies and likely induced anatexis. We suggest, therefore, that the older Lu-Hf age of AME18-138 estimates the timing of initial garnet growth at 3390 ± 37 Ma. The younger Sm-Nd age at 3307 ± 14 Ma agrees with the age of the enveloping Emu Pool supersuite granites. Most likely, the heat related to the Emu Pool activity heated this rock above the Sm-Nd closure temperature, and reset the Sm-Nd age at 3307 ± 14 Ma.

Table 2
Lu-Hf and Sm-Nd isotope data.

Sample [a]	Lu (ppm)	Hf (ppm)	$^{176}Lu/^{176}Hf$ [b]	$^{176}Hf/^{177}Hf$	±	εHf(0) [c]	εHf(i) [c]	Sm (ppm)	Nd (ppm)	$^{147}Sm/^{144}Nd$ [b]	$^{143}Nd/^{144}Nd$	±	εNd(0) [d]	εNd(i) [d]
AME18-028 *(Lu-Hf: 3418 ± 28 Ma, Sm-Nd: 3173 ± 14 & 2940 ± 71 Ma U-Pb: 3445 ± 36 Ma)*														
WRB	0.188	1.79	0.0145	0.281509	15	−45.1	−0.6	2.19	11.4	0.1157	0.510745	28	−36.9	−3.8
WRS	0.177	1.91	0.0131	0.281415	14	−48.4	−0.8	2.15	11.2	0.1157	0.510751	26	−36.8	−3.7
G1	1.44	3.57	0.0573	0.284328	20	+54.6	−0.7	2.30	5.40	0.2580	0.513553	26	+17.9	−5.4
G2	1.36	3.71	0.0521	0.283973	14	+42.0	−1.2	2.34	5.53	0.2559	0.513462	27	+16.1	−6.4
G3	1.36	3.69	0.0524	0.283997	14	+42.9	−0.9	2.29	5.29	0.2613	0.513580	26	+18.4	−6.1
G4	1.42	3.82	0.0527	0.284048	14	+44.7	+0.1	2.27	5.25	0.2616	0.513541	26	+17.6	−7.0
G1L[e]								1.09	0.76	0.8705	0.526598	30	+272.3	−3.3
G2L[e]								1.04	0.74	0.8510	0.526144	36	+263.5	−4.2
AME18-031 *(Lu-Hf: 3321 ± 17 Ma, Sm-Nd: N/A, U-Pb: N/A)*														
WRB	0.574	4.04	0.0202	0.281929	15	−30.3	+0.1	5.59	17.1	0.1975	0.511920	28		
WRS	0.567	3.91	0.0206	0.281959	16	−29.2	+0.3	4.70	14.9	0.1908	0.513061	27		
G1	3.47	2.34	0.2108	0.294186	15	+403.2	+2.4	2.69	7.89	0.2061	0.512830	29		
G2	3.58	2.55	0.1999	0.293398	15	+375.3	−0.9	2.60	7.20	0.2185	0.512851	46		
G3								2.62	7.56	0.2099	0.512902	32		
G4	3.78	2.41	0.2225	0.294833	16	+426.0	−1.2	2.15	7.42	0.1756	0.513017	27		
AME18-053H *(Lu-Hf: 3337 ± 11 Ma, Sm-Nd: 3317 ± 17 & 3246 ± 32 Ma, U-Pb: 3455 ± 35 Ma)*														
WRB1	0.274	3.54	0.0110	0.281266	14	−53.7	−2.4	2.86	13.5	0.1279	0.511209	27	−27.9	+1.5
WRS	0.278	3.58	0.0110	0.281300	15	−52.5	−1.2	2.92	13.8	0.1275	0.511194	27	−28.2	+1.5
WRB2	0.295	3.78	0.0111	0.281301	14	−52.5	−1.3	2.94	13.9	0.1281	0.511207	27	−27.9	+1.4
G1								4.78	12.6	0.2278	0.513338	26	13.7	0.6
G2	5.50	1.18	0.7243	0.327055	17	+1565.5	−4.6	3.97	9.95	0.2504	0.513836	27	23.4	0.9
G3	4.72	0.89	0.7614	0.329424	17	+1649.3	−5.2	4.81	13.1	0.2219	0.513215	26	+11.3	+0.7
G4								4.93	13.6	0.2190	0.513163	27	+10.2	+0.9
G5	4.42	1.08	0.5848	0.318264	16	+1254.6	+1.5	4.41	12.1	0.2207	0.513196	27	+10.9	+0.8
G6	4.52	1.09	0.5939	0.318797	16	+1273.5	−0.2	4.74	13.5	0.2121	0.513013	26	+7.3	+0.9
G7	4.91	1.04	0.6784	0.324150	17	+1462.8	−3.0	4.30	11.4	0.2277	0.513345	27	+13.8	+0.8
G8	4.56	1.13	0.5742	0.317555	16	+1229.6	+0.6	4.42	12.0	0.2219	0.513230	26	+11.5	+1.0
G1L[e]								1.80	1.76	0.6184	0.521974	28	+182.1	+1.8
G2L[e]								1.99	2.18	0.5545	0.520549	28	154.3	1.3
AME18-058 *(Lu-Hf: 3298 ± 35 Ma, Sm-Nd: 3252 ± 15 & 2835 ± 17 Ma, U-Pb: 3461 ± 21 Ma)*														
WRB	0.473	4.55	0.0148	0.281531	14	−44.3	−2.0	3.79	17.5	0.1309	0.511135	29	−29.3	−1.7
WRS	0.482	4.51	0.0152	0.281578	15	−42.7	−1.4	3.79	17.5	0.1307	0.511149	28	−29.0	−1.4
G1	2.38	3.83	0.0882	0.286208	15	+121.0	−1.6	2.64	6.02	0.2650	0.513658	27	+19.9	−5.1
G2	2.37	3.95	0.0853	0.286036	15	+115.0	−1.0	2.92	7.47	0.2366	0.513117	28	+9.3	−5.3
G3	2.48	3.89	0.0903	0.286247	15	+122.4	−5.0	2.47	5.64	0.2645	0.513630	31	+19.3	−5.4
G4	2.28	3.86	0.0839	0.285911	15	+110.5	−2.6	2.71	6.28	0.2523	0.513427	27	+15.4	−4.9
G1L[e]								1.30	1.01	0.7821	0.525133	29	+243.7	−1.8
G2L[e]								1.27	0.97	0.7964	0.525463	30	+250.2	−1.3
AME18-060 *(Lu-Hf: 3411 ± 53 Ma, Sm-Nd: 3358 ± 13 & 3033 ± 44 Ma, U-Pb: 3440 ± 35 Ma)*														
WRB	0.510	6.49	0.0112	0.281377	14	−49.8	+2.4	2.32	10.2	0.1366	0.511239	27	−27.3	−1.2
G1	2.89	4.66	0.0880	0.286395	15	+127.7	+1.1	2.96	7.79	0.2215	0.512942	26	+5.9	−4.9
G2								3.16	8.58	0.2228	0.512990	27	+6.9	−3.4
G3	3.10	4.52	0.0973	0.287087	15	+152.1	+4.0	2.96	7.79	0.2295	0.513124	27	+9.5	−3.4
G4	2.82	4.99	0.0801	0.285884	15	+109.6	+1.5	3.28	9.55	0.2080	0.512660	26	+0.4	−4.0
Cld	0.842	4.64	0.0257	0.282318	15	−16.5	+1.8	13.01	62.1	0.1266	0.511060	26	−30.8	−0.3
G1L[e]								1.03	0.38	1.6265	0.544335	34	+618.3	−3.1
G2L[e]								1.09	0.40	1.6792	0.545527	37	+641.6	−2.7
AME18-080 *(Lu-Hf: N/A, Sm-Nd: 3282 ± 39 Ma, U-Pb: 3452 ± 40 Ma)*														
WRB								1.38	6.50	0.1287	0.511010	26	−31.8	−3.0
WRS								1.31	6.16	0.1286	0.510997	29	−32.0	−3.2
G1								1.43	3.97	0.2184	0.512967	26	+6.4	−2.8
G2								1.42	3.48	0.2468	0.513592	27	+18.6	−2.6
G3								1.34	3.13	0.2601	0.513827	26	+23.2	−3.7
AME18-138 *(Lu-Hf: 3390 ± 11 Ma, Sm-Nd: 3307 ± 14 & 2987 ± 82 Ma, U-Pb: N/A)*														
WRB	0.548	2.26	0.0344	0.282852	14	+2.4	+0.4	3.00	10.0	0.1812	0.512339	27	−5.8	+0.8
WRS								2.73	9.04	0.1828	0.512400	26	−4.6	+1.3
G1								4.37	9.99	0.2646	0.513880	27	+24.2	−1.9
G2								3.93	7.30	0.3258	0.515154	26	+49.1	−0.6
G3								4.15	8.30	0.3023	0.514654	26	+39.3	−1.3
G4								3.71	6.35	0.3533	0.515740	26	+60.5	+0.3
G5	1.61	2.80	0.0816	0.285945	15	+111.7	+0.9	3.37	6.42	0.3177	0.515039	26	+46.8	+0.3
G6	1.80	2.67	0.0954	0.286826	15	+142.9	+0.1	3.38	6.11	0.3351	0.515381	26	+53.5	+0.3
G7	1.80	2.90	0.0878	0.286353	21	+126.2	+1.0	3.48	6.81	0.3096	0.514870	27	+43.5	+0.1
G7	1.77	3.05	0.0823	0.285977	15	+112.9	+0.4	3.19	5.32	0.3629	0.515950	26	+64.6	+0.7
G1L[e]								2.05	1.05	1.1940	0.534495	32	+426.4	+1.0
G2L[e]								0.94	0.47	1.2174	0.535009	32	+436.4	+1.1

Hf isotope data is normalized to JMC475 value of 0.282160 (Vervoort and Blichert-Toft, 1999).

[a] G (#), garnet fraction (number); WRB (#), whole-rock bomb dissolution (number); WRS; whole-rock Savillex dissolution; Cld, chloritoid fraction; LM, light mineral fraction; GL (#), garnet fraction leached in H_2SO_4 (number).

[b] Precision on parent/daughter ratio determined to be 0.5% based on the long-term reproducibility of rock standards in the WSU lab as described by Bouvier et al. (2008).

[c] Epsilon Hf values determined using $^{176}Hf/^{177}Hf$ of $CHUR_{(0)} = 0.282785$, $^{176}Lu/^{177}Lu = 0.0336$ (Bouvier et al., 2008), and the ^{176}Lu decay constant of $1.867x10^{-11}$ yr^{-1} (Söderlund et al., 2004; Scherer et al., 2001).

[d] Epsilon Nd values determined using $^{143}Nd/^{144}Nd$ of $CHUR_{(0)} = 0.512630$, $^{147}Nd/^{144}Nd = 0.1960$ (Bouvier et al., 2008), and the ^{147}Sm decay constant of $6.54x10^{-12}$ yr^{-1} (Lugmair and Marti, 1978).

[e] Lu-Hf values are not determined for the garnet aliquots leached in H_2SO_4.

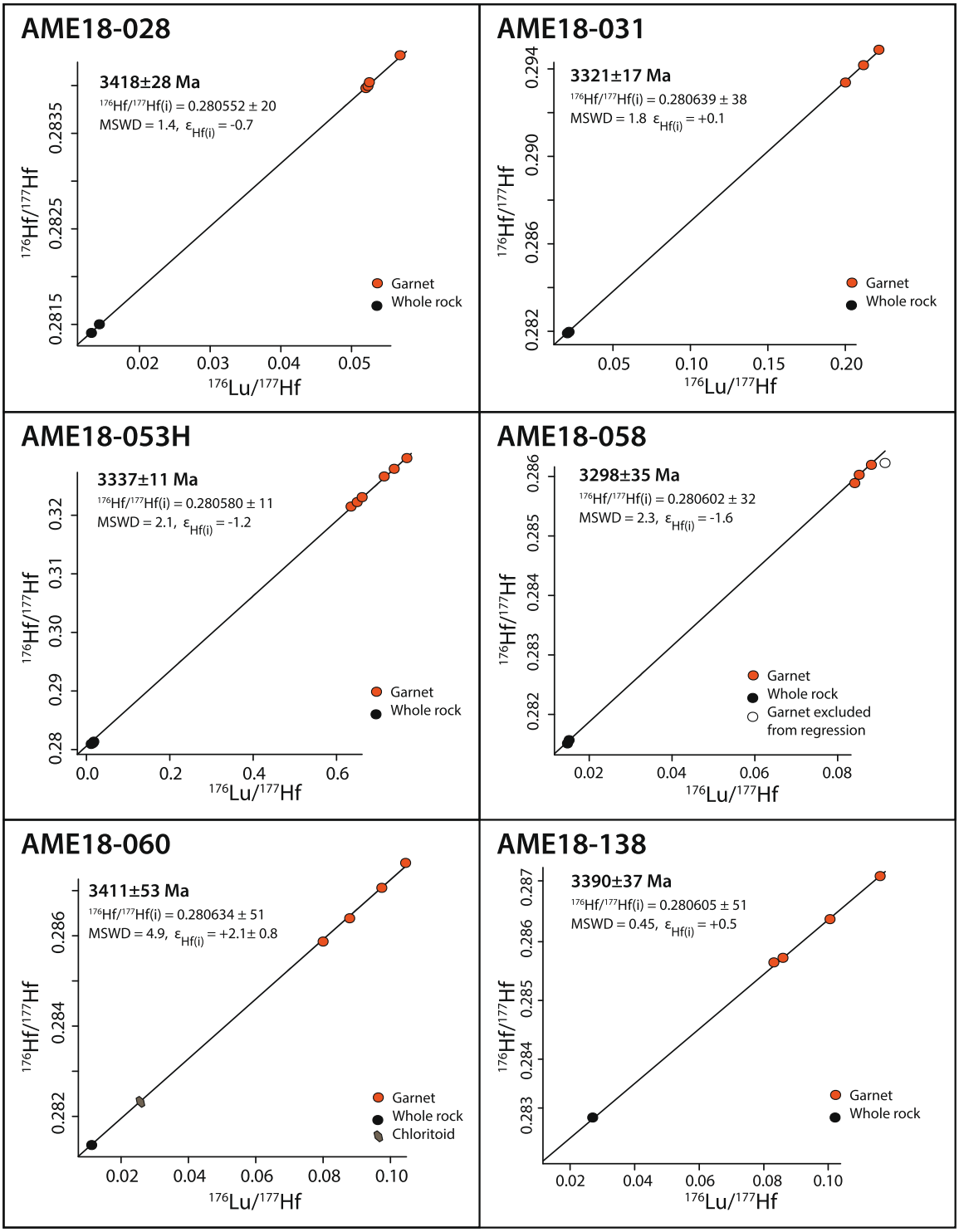

Fig. 8. Garnet Lu-Hf isochrons at 2SE precision.

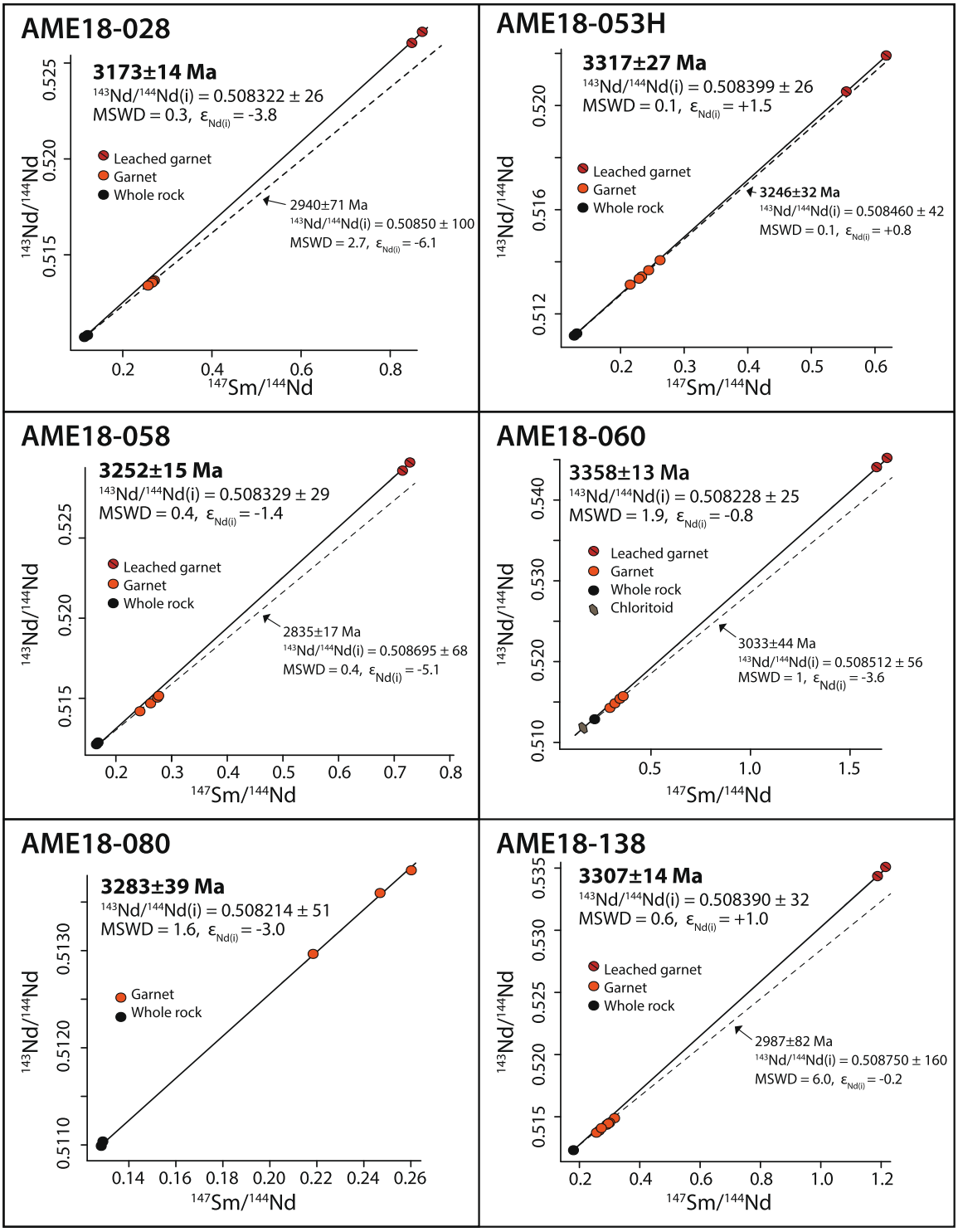

Fig. 9. Garnet Sm-Nd isochrons at 2SE precision. The solid red circles represent garnet aliquots not treated with sulfuric acid before final digestion, while the hatched red circles represent the treated aliquots. The solid lines are the isochrons calculated using the treated aliquots, and the dashed lines are the isochrons determined with the untreated aliquots.

In contrast, the offset between the Lu-Hf and Sm-Nd ages of sample AME18-028 is not easily explained by differences in the Lu-Hf and Sm-Nd closure temperatures in garnet. The metamorphic mineral assemblage and textures in this sample do not provide any evidence for a later reheating event above the closure temperature of the Sm-Nd system. Further, there are no known thermal or igneous events in the Pilbara at ~ 3.13 Ga which could have reset the Sm-Nd age of this rock. We interpret the offset in AME18-028 between the sulfuric treated Sm-Nd and Lu-Hf ages to reflect the incomplete removal of younger LREE accessory minerals by sulfuric acid leaching.

In total, the garnet ages indicate two discrete episodes of garnet growth: at ~ 3.42 Ga (3418 ± 28 to 3390 ± 37 Ma), and at ~ 3.33 Ga (3337 ± 11 to 3298 ± 35 Ma). These two periods are broadly consistent with the ages of the Tambina and Emu Pool granitic supersuites, which

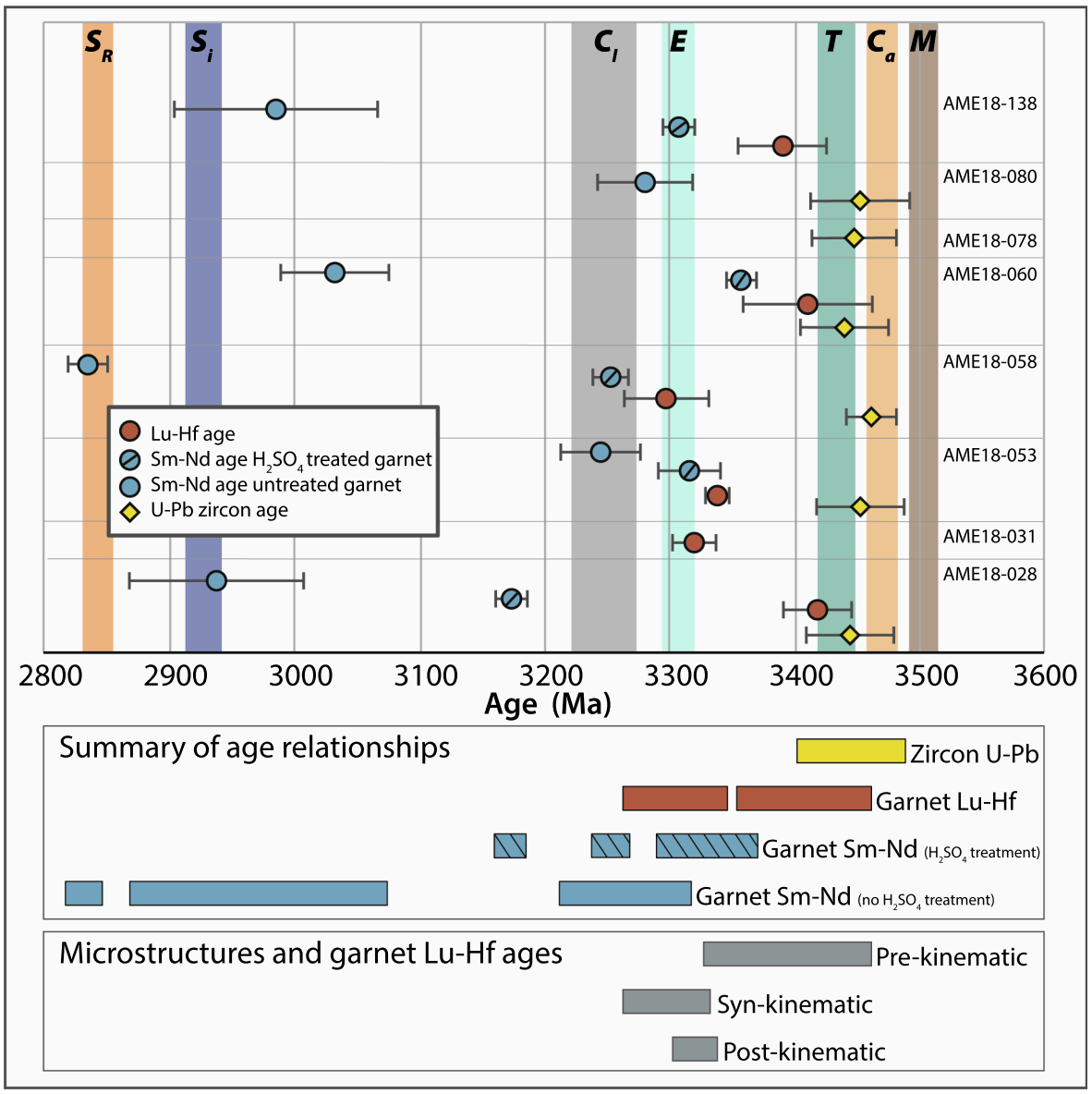

Fig. 10. The relationships between the geochronologic and microstructural data presented in this study with 2SE precision. The top panel shows zircon U-Pb, and garnet Lu-Hf and Sm-Nd ages determined for these samples. Note that two Sm-Nd ages are plotted for each sample; one using the aliquots treated with H_2SO_4 (hatched) and one using the untreated garnet aliquots (open circle). The ages of the major granitic supersuites are also overlain in the top panel as vertical bars; M) Mulgundoona, C_a) Callina, T) Tambina, E) Emu Pool, C_l) Cleland, S_i) Sisters, S_R) Split rock. The bars in the middle panel represent the groups of age data. Note the two discrete groups of garnet Lu-Hf ages highlighted in the text. The bottom panel shows the relationship between the Lu-Hf ages of these samples, and their microstructures as either Pre-, Syn-, or Post-fabric development.

has been suggested to coincide with the timing of important dome-forming event in the East Pilbara Terrane (Williams and Collins, 1990; Collins et al., 1998; Collins and Van Kranendonk, 1999; Van Kranendonk et al., 2007; Wiemer et al., 2018).

The Sm-Nd ages of these samples are affected to varying degrees by younger LREE mineral inclusions and reheating above the Sm-Nd closure temperature. Although imprecise, the unleached Sm-Nd ages of AME18-138, 060, 058, and 028 reflect resetting of the LREE-rich minerals in these rocks at ~ 3.00 to 2.83 Ga. This age range broadly agrees with the ages of the Sisters and Split Rock granitic supersuites and has been associated with "reamplification" of the Paleoarchean dome-and-keel structures later in the Mesoarchean (Van Kranendonk et al., 2006).

5.4. Garnet growth in relation to the age of fabric development

Interpreting the significance of the garnet Lu-Hf ages requires documentation of the relationship of the garnets to the structural fabric within the Warrawoona Syncline. This dominant structural fabric in the Warrawoona Syncline has been associated with the formation of the Mt Edgar dome (e.g., Collins, 1989; Collins, 1998; Kloppenburg et al., 2001; Van Kranendonk et al., 2004), so the timing of this fabric development is implicitly related to the timing of a dome formation event. There are two stages of garnet growth in these samples, at ~ 3.42 Ga and ~ 3.33 Ga. Of these, garnet in the older group of samples (AME18-028, 060, 138) all have pre-kinematic microstructures (Fig. 10, Appendix 4). In these samples, garnet is anhedral and disaggregated, often forming patchy networks which are elongate with the dominant foliation fabric. In

addition, orientations of the inclusions in garnet are discordant with the matrix fabric. Together, these textural relationships indicate that garnet growth in these samples occurred before development of the dominant structural fabric. These microstructural observations are consistent with the geochronology, as these samples are all in the older group of Lu-Hf ages. Growth of garnet in these samples likely corresponds to an earlier stage of fabric development, before the development of the current dominant fabric in the Warrawoona Syncline.

Garnet in the younger ~ 3.34 Ga group have a variety of textures that range from pre- to post-fabric development (Fig. 7). In sample AME18-053 (Lu-Hf age 3337 ± 11 Ma), the matrix fabric is bent around garnet, indicating that garnet is pre- or *syn*-kinematic. The subhedral garnet shape and lack of a discernable internal fabric defined by quartz and ilmenite inclusions, suggest that the garnet in this sample predates the major phase of fabric development.

Garnet in AME18-058XZ (Lu-Hf age 3298 ± 35 Ma) is also porphyroblastic, with the matrix fabric wrapped around it. In contrast to AME18-053, however, garnet in this sample has well-defined quartz inclusion bands and strongly aligned ilmenite needles, indicating that garnet overgrew a pre-existing fabric. Further, the curved nature of the quartz inclusion bands and the higher angle of ilmenite needles at the garnet core indicate that the garnet progressively rotated clockwise in a manner consistent with the asymmetric top-to-the-right sigmoidal shape of the garnet. These microstructures suggest that the garnet growth in this sample was synkinematic.

Garnet in AME18-031 (Lu-Hf age 3321 ± 17 Ma) are interpreted as late- or post-tectonic, based on their euhedral shape, the lack of any fabric deflection, and the observation that the ilmenite seams that define the fabric are included in garnet without disruption. This variety of garnet microstructures observed in samples with overlapping Lu-Hf ages at ~ 3.33 Ga, indicates that the dominant foliation developed within that time interval. Thus, 3.33 Ga is our best estimate for the beginning of a significant doming event In the Mt. Edgar Granitic Complex.

5.5. *The timescales of the formation of dome-and-keel structures in the Paleoarchean*

The existing picture about the timescales of dome formation in the Pilbara comes from multiple observations: (1) the assumed connection between the granitic supersuites and the doming process (e.g., Van Kranendonk et al., 2002, 2007); (2) the relationships between deformed rocks and the absolute ages of crosscutting dikes and of rocks above angular unconformities (Collins 1989; Collins et al., 1998; Van Kranendonk et al., 2004); and (3) from the absolute ages of metamorphic minerals taken to represent the timing of deformation and doming (François et al., 2014; Wiemer et al., 2018). The totality of evidence indicates that the final architecture of the Pilbara dome-and-keel structures is the result of multiple doming events occurring over hundreds of millions of years. Our results are consistent with the timing of at least two of these previously described dome-forming events. The earliest evidence for doming in our dataset is represented by the older population of Lu-Hf garnet ages, at ~ 3.42 Ga (3418 ± 28 to 3390 ± 37 Ma). Garnet growth in these older samples predates the development of the dominant structural fabric in the Warrawoona Syncline and may be connected to the deformation that also resulted in the angular unconformity between the Panorama formation and overlying Kelly Group at ~ 3.42 Ga (Van Kranendonk et al., 2004).

This older group of garnet Lu-Hf ages also provides insight about the time interval between the eruption of the protolith and the onset of P-T conditions related to garnet growth. Most of these samples have zircon U-Pb ages consistent with their eruption with the Duffer formation at 3.46 Ga (Amelin et al., 2000; Kemp et al., 2015). Consequently, these rocks must have been buried to garnet stability conditions ~ 30 m.y. after their eruption. This timing estimate is consistent with P-T modeling by François et al. (2014) and Sizova et al. (2018), in which rocks in the Warrawoona Syncline were quickly "sagducted" to pressures>8 kbar.

The younger group of Lu-Hf ages, at ~ 3.33 Ga (3337 ± 11 and 3298 ± 35 Ma), agrees with the previous estimates for the "main phase" of doming in the Mt. Edgar complex related to the emplacement of the Emu Pool granitic supersuite (Van Kranendonk et al., 2004). Our data further indicate that the Emu Pool magmatism was responsible for the development of the dominant fabrics in the Warrawoona Syncline, as some garnet in this younger group have late- to post-kinematic microstructures (e.g., AME18-031). No microstructural data are available for interpreting the significance of the younger Sm-Nd ages in relation to fabric development or dome formation. It is likely, however, that the array of younger Sm-Nd ages reflects the re-equilibration of younger LREE-rich accessory minerals in these rocks that are sensitive to lower temperature thermal disturbances, rather than primary garnet growth. Therefore, these phosphate minerals may record the continued thermal effects of the Cleland Supersuite after the Emu Pool event (e.g., AME-080 and 053, 3324 to 3277 Ma). This is in line with Roberts et al. (2022) who suggest that Cleland magmatism drove further dome amplification in the Mt. Edgar complex.

The youngest Sm-Nd ages range to about 2.8 Ga, which significantly post-dates the primary dome forming events in the Paleoarchean. These young ages are consistent with the Sisters (2954–2919 Ma) and Split Rock (2851–2831 Ma) supersuites, which have also been attributed to later amplification of the domes (Van Kranendonk et al., 2006).

This paper demonstrates the utility of integrating garnet geochronology and microstructural analyses. This approach helps to establish the temporal connections between metamorphism, deformation, and igneous activity in Paleoarchean dome-and-keel structures. The data in our study show that growth of garnet, and development of fabric, in the Warrawoona Syncline occurred simultaneously with the timing of crustal overturn events. Our data, along with previous work, demonstrate that there were several such events throughout the Paleoarchean, and these overturn events were important for creating preservable felsic crust on early Earth. Although these results are locally applicable to the Pilbara Craton, it is likely that this style of crust formation applies to other Archean dome-and-keel terranes.

Cutts et al. (2014) took a similar approach to ours with the dome-and-keel structures in the Barberton Greenstone Belt. They documented two discrete metamorphic events at approximately 3.43 and 3.23 Ga, both of which coincide with ages of granitic intrusions in the region. These relationships between metamorphism and plutonic activity are remarkably similar to our observations in the Pilbara Craton. This consistency provides tantalizing evidence that the metamorphic and deformational histories of other dome-and-keel terranes may also reflect this style of multiple punctuated crustal overturn events. If so, crustal overturn would be a globally important process for making Archean continental crust on the early Earth.

6. Conclusions

Our study uses garnet geochronology to constrain the timescales of deformation in the Warrawoona Syncline related to doming and crustal overturn. We demonstrate that garnet Lu-Hf and Sm-Nd geochronology can be integrated with microstructural analyses to identify two discrete doming events in the Warrawoona Syncline and Mt. Edgar Granitic Complex, at ~ 3.42 Ga (3418 ± 28 to 3390 ± 37 Ma) and at ~ 3.33 Ga (3337 ± 11 to 3298 ± 35 Ma). In addition, our zircon Hf isotope data indicate the volcanic protoliths of these samples were juvenile crustal additions. This study complements other recent work that has demonstrated that the granitic and volcanic rocks in the Pilbara are largely juvenile crustal additions from the mantle, without significant contributions from Eoarchean or Hadean crust (Petersson et al., 2019, 2020; Salerno et al., 2021; Kemp et al., 2023). Consequently, Paleoarchean crustal overturn events and the origin of dome-and-keel structures are likely closely linked with the formation of new continental crust.

CRediT authorship contribution statement

Ross Salerno Conceptualization, Validation, Formal analysis, Investigation, Resources, Data curation, Writing – original draft, Visualization. **Nicolas Roberts:** Conceptualization, Validation, Formal analysis, Investigation, Resources, Data curation, Writing – original draft, Visualization. **Jeffrey Vervoort:** Conceptualization, Methodology, Validation, Resources, Writing – review & editing, Supervision, Project administration, Funding acquisition. **Basil Tikoff:** Conceptualization, Methodology, Validation, Resources, Writing – review & editing, Supervision, Project administration, Funding acquisition.

Declaration of Competing Interest

The authors declare the following financial interests/personal relationships which may be considered as potential competing interests: Ross Salerno reports financial support was provided by National Science Foundation.

Data availability

Our data are attached as an appendix to this paper

Acknowledgements

We would like to acknowledge Charles Knaack, Peter Baker, and Chao Zhang for laboratory and technical support at WSU. Thanks to Rex Key and Casey Idzikowski of UW Madison for their assistance in the field. We also thank the Brooks family and the staffs of Limestone Station and Corunna Downs Station for their help with logistics in the field. Thanks to Steve Sheppard and Calidus Resources Ltd for land access and guidance in sample targeting. This project was supported with funding from the NSF grants EAR 2020831 to JV and EAR 2020057 to BT and a grant from the Wisconsin Alumni Research Foundation to BT. We are grateful for the helpful comments from three anonymous reviewers and from Daniel Wiemer. JV acknowledges support from the Gledden Visiting Researcher Fellowship from the University of Western Australia.

Appendix A. Supplementary material

Supplementary data to this article can be found online at https://doi.org/10.1016/j.precamres.2023.107108.

References

Amelin, Y., Lee, D.C., Halliday, A.N., 2000. Early-middle Archaean crustal evolution deduced from Lu-Hf and U-Pb isotopic studies of single zircon grains Geochim. Cosmochim. Acta 64 (24), 4205–4225. https://doi.org/10.1016/S0016-7037(00)00493-2.

Anczkiewicz, R., Thirlwall, M.F., 2003. Improving precision of Sm-Nd garnet dating by H2SO4 Leaching: a simple solution to the phosphate inclusion problem. Geol. Soc. London, Special Publicat. 220, 83–91.

Armstrong, R.L., 1981. Radiogenic isotopes: the case for crustal recycling on a near steady-state no continental growth Earth. Phil. Trans. Roy. Soc. Lond. A 301, 443.

Bickle, M.J., Bettenay, L.F., Chapman, H.J., Groves, D.I., McNaughton, N.J., Campbell, I. H., de Laeter, J.R., 1993. Origin of the 3500–3300 Ma calc-alkaline rocks in the Pilbara Archaean: isotopic and geochemical constraints from the Shaw Batholith. Precambr. Res. 60, 117–149. https://doi.org/10.1016/0301-9268(93)90047-6.

Blichert-Toft, J., Albarède, F., Kornprobst, J., 1999. Lu-Hf Isotope Systematics of Garnet Pyroxenites from Beni Bousera, Morocco: Implications for Basalt Origin. Science 283, 1303–1306. https://doi.org/10.1126/science.283.5406.1303.

Bouvier, A., Vervoort, J.D., Patchett, P.J., 2008. The Lu-Hf and Sm-Nd isotopic composition of CHUR: Constraints from unequilibrated chondrites and implications for the bulk composition of terrestrial planets. Earth Planet. Sci. Lett. 273, 48–57. https://doi.org/10.1016/j.epsl.2008.06.010.

Caddick, M.J., Konopásek, J., Thompson, A.B., 2010. Preservation of garnet growth zoning and the duration of prograde metamorphism. J. Petrol. 51, 2327–2347. https://doi.org/10.1093/petrology/egq059.

Champion, D.C., Smithies, R.H., 2007. Chapter 4.3 Geochemistry of Paleoarchean Granites of the East Pilbara Terrane, Pilbara Craton, Western Australia: Implications for Early Archean Crustal Growth. Dev. Precambrian Geol. 15, 369–409. https://doi.org/10.1016/S0166-2635(07)15043-X.

Cheng, H., King, R.L., Nakamura, E., Vervoort, J.D., Zhou, Z., 2008. Coupled Lu-Hf and Sm-Nd geochronology constrains garnet growth in ultra-high-pressure eclogites from the Dabie orogen. J. Metamorph. Geol. 26, 741–758. https://doi.org/10.1111/j.1525-1314.2008.00785.x.

Collins, W.J., 1989. Polydiapirism of the Archean Mount Edgar Batholith, Pilbara Block. Western Australia. Precambrian Res. 43, 41–62. https://doi.org/10.1016/0301-9268(89)90004-1.

Collins, W.J., Van Kranendonk, M.J., Teyssier, C., 1998. Partial convective overturn of Archaean crust in the east Pilbara Craton, Western Australia: Driving mechanisms and tectonic implications. J. Struct. Geol. 20, 1405–1424. https://doi.org/10.1016/S0191-8141(98)00073-X.

Collins, W.J., Van Kranendonk, M.J., 1999. Model for the development of kyanite during partial convective overturn of Archean granite-greenstone terranes: The Pilbara Craton. Australia. J. Metamorph. Geol. 17, 145–156. https://doi.org/10.1046/j.1525-1314.1999.00187.x.

Condie, K.C., 1981. Archean Granite-Greenstone Terranes. In: Condie, K.C. (Ed.), Archean Greenstone Belts, Developments in Precambrian Geology. Elsevier, Amsterdam, pp. 1–44 https://doi.org/https://doi.org/10.1016/S0166-2635(08)70074-4.

Condie, K.C., Aster, R.C., 2010. Episodic zircon age spectra of orogenic granitoids: The supercontinent connection and continental growth. Precambr. Res. 180, 227–236. https://doi.org/10.1016/j.precamres.2010.03.008.

Cutts, K.A., Stevens, G., Hoffmann, J.E., Buick, I.S., Frei, D., Münker, C., 2014. Paleo- to mesoarchean polymetamorphism in the barberton granite-greenstone belt, south africa: Constraints from U-Pb monazite and Lu-Hf garnet geochronology on the tectonic processes that shaped the belt. Bull. Geol. Soc. Am. 126, 251–270. https://doi.org/10.1130/B30807.1.

de Wit, M.J., Jones, M.G., Buchanan, D.L., 1992. The geology and tectonic evolution of the Pietersburg Greenstone Belt. South Africa 55, 123–153.

DePaolo, D.J., 1981. Neodymium isotopes in the Colorado Front Range and crust-mantle evolution in the Proterozoic. Nature 291, 193–196. https://doi.org/10.1038/291193a0.

Duchêne, S., Blichert-Toft, J., Luais, B., Télouk, P., Lardeaux, J.-M., Albarède, F., 1997. The Lu–Hf dating of garnets and the ages of the Alpine high-pressure metamorphism. Nature 387, 586–589. https://doi.org/10.1038/42446.

Fisher, C.M., Hanchar, J.M., Samson, S.D., Dhuime, B., Blichert-Toft, J., Vervoort, J.D., Lam, R., 2011. Synthetic zircon doped with hafnium and rare earth elements: A reference material for in situ hafnium isotope analysis. Chem. Geol. 286, 32–47. https://doi.org/10.1016/j.chemgeo.2011.04.013.

Fisher, C.M., Vervoort, J.D., Hanchar, J.M., 2014. Guidelines for reporting zircon Hf isotopic data by LA-MC-ICPMS and potential pitfalls in the interpretation of these data. Chem. Geol. 363, 125–133. https://doi.org/10.1016/j.chemgeo.2013.10.019.

Fisher, C.M., Vervoort, J.D., 2018. Using the magmatic record to constrain the growth of continental crust—The Eoarchean zircon Hf record of Greenland. Earth Planet. Sci. Lett. 488, 79–91. https://doi.org/10.1016/j.epsl.2018.01.031.

François, C., Philippot, P., Rey, P., Rubatto, D., 2014. Burial and exhumation during Archean sagduction in the East Pilbara Granite-Greenstone Terrane. Earth Planet. Sci. Lett. 396, 235–251. https://doi.org/10.1016/j.epsl.2014.04.025.

Fyfe, W.S., 1978. The evolution of the earth's crust: Modern plate tectonics to ancient hot spot tectonics? Chem. Geol. 23, 89–114. https://doi.org/10.1016/0009-2541(78)90068-2.

Goodge, J.W., Vervoort, J.D., 2006. Origin of Mesoproterozoic A-type granites in Laurentia: Hf isotope evidence. Earth Planet. Sci. Lett. 243, 711–731. https://doi.org/10.1016/j.epsl.2006.01.040.

Gruau, G., Jahn, B.M., Glikson, A.Y., Davy, R., Hickman, A.H., Chauvel, C., 1987. Age of the Archean Talga-Talga Subgroup, Pilbara Block, Western Australia, and early evolution of the mantle: new SmNd isotopic evidence. Earth Planet. Sci. Lett. 85, 105–116. https://doi.org/10.1016/0012-821X(87)90025-2.

Hämmerli, J., Kemp, A.I.S., Spandler, C., 2014. Neodymium isotope equilibration during crustal metamorphism revealed by in situ microanalysis of REE-rich accessory minerals. Earth Planet. Sci. Lett. 392, 133–142. https://doi.org/10.1016/j.epsl.2014.02.018.

Hermann, J., Rubatto, D., 2003. Relating zircon and monazite domains to garnet growth zones: Age and duration of granulite facies metamorphism in the Val Malenco lower crust. J. Metam. Geol. 21, 833–852. https://doi.org/10.1046/j.1525-1314.2003.00484.x.

Hickman, A.H., 1983. Geology of the Pilbara Block and its environs. Geological Survey of Western Australia, Perth 127, 268.

Hickman, A.H., 1984. Archaean diapirism in the Pilbara Block, Western Australia. In: Kroner, A., Greiling, R. (Eds.), Precambrian Tectonics Illustrated, E. Schweizerbart sche, Stuttgart, Germany, pp. 113–127.

Hickman, A.H., 2012. Review of the Pilbara Craton and Fortescue Basin, Western Australia: Crustal evolution providing environments for early life. Isl. Arc. 21, 1–31. https://doi.org/10.1111/j.1440-1738.2011.00783.x.

Hickman, A.H., 2021. East Pilbara Craton: a record of one billion years in the growth of Archean continental crust. Geological Survey of Western Australia Report 143.

Hofmann, A., 1988. Chemical differentiation of the Earth: the relationship between mantle, continental crust, and oceanic crust. Earth Planet. Sci. Lett. 90, 297–314.

Jahn, B.M., Glikson, A.Y., Peucat, J.J., Hickman, A.H., 1981. REE geochemistry and isotopic data of Archean silicic volcanics and granitoids from the Pilbara Block, Western Australia: implications for the early crustal evolution. Geochim. Cosmochim. Acta 45, 1633–1652. https://doi.org/10.1016/S0016-7037(81)80002-6.

Johnson, T.A., Vervoort, J.D., Ramsey, M.J., Aleinikoff, J.N., Southworth, S., 2018. Constraints on the timing and duration of orogenic events by combined Lu–Hf and

Sm–Nd geochronology: An example from the Grenville orogeny. Earth Planet. Sci. Lett. 501, 152–164. https://doi.org/10.1016/j.epsl.2018.08.030.
Kemp, A.I.S., Hickman, A.H., Kirkland, C.L., Vervoort, J.D., 2015. Hf isotopes in detrital and inherited zircons of the Pilbara Craton provide no evidence for Hadean continents. Precambrian Res. 261, 112–126. https://doi.org/10.1016/j.precamres.2015.02.011.
Kemp, A.I.S., Vervoort, J.D., Petersson, A., Hugh Smithies, R., Lu, Y., 2023. A linked evolution for granite-greenstone terranes of the Pilbara Craton from Nd and Hf isotopes, with implications for Archean continental growth. Earth Planet. Sci. Lett. 601 https://doi.org/10.1016/j.epsl.2022.117895.
Kloppenburg, A., White, S.H., Zegers, T.E., 2001. Structural evolution of the Warrawoona Greenstone Belt and adjoining granitoid complexes, Pilbara Craton, Australia: Implications for archaean tectonic processes. Precambrian Res. 112, 107–147. https://doi.org/10.1016/S0301-9268(01)00172-3.
Lugmair, G.W., Marti, K., 1978. Lunar initial 143Nd/144Nd: Differential evolution of the lunar crust and mantle. Earth Planet. Sci. Lett. 39, 349–357.
Mackey, T.E., Richardson, L.M., 1997. Airborne gamma-ray spectrometry colour composite pixel-image map of Marble Bar, scale 1:250 000. Australian Geological Survey. Organization.
Mareschal, J., West, G., 1980. A model for Archean tectonism. Part 2. Numerical models of vertical tectonism in greenstone belts. Can. J. Earth Sci. 17, 60–71.
McLennan, S.M., Hemming, S., McDaniel, D.K., Hanson, G.N., 1993. Geochemical approaches to sedimentation, provenance, and tectonics. In: Johnsson, M.J., Basu, A. (Eds.), Processes Controlling the Composition of Clastic Sediments Geological Society of America Special Paper 284. Geological Society of America, pp. 21–40. https://doi.org/10.1130/SPE284-p21.
Mezger, K., Essene, E.J., Halliday, A.N., 1992. Closure temperatures of the Sm-Nd system in metamorphic garnets. In Earth and Planetary Science Letters. 113, 397–409.
Murphy, D.T., Wiemer, D., Bennett, V.C., Spring, T., Trofimovs, J., Cathey, H.E., 2021. Paleoarchean variole-bearing metabasalts from the East Pilbara Terrane formed by hydrous fluid phase exsolution and implications for Archean greenstone belt magmatic processes. Precambr. Res. 357, 106114 https://doi.org/10.1016/j.precamres.2021.106114.
Nelson, D. R., 1999. Compilation of geochronology data, 1998. Geol. Surv. West. Aust. Rec. 1999/2, 222 p.
Otamendi, J.E., de la Rosa, J.D., Patiñ Douce, A.E., Castro, A., 2002. Rayleigh fractionation of heavy rare earths and yttrium during metamorphic garnet growth. Geology 30, 159–162. https://doi.org/10.1130/0091-7613(2002)030<0159:RFOHRE>2.0.CO;2.
Patchett, J.P., Arndt, N.T., 1986. Nd isotopes and tectonics of 1.9-1.7 Ga crustal genesis. Earth Planet. Sci. Lett. 78, 329–338. https://doi.org/10.1016/0012-821X(86)90001-4.
Pawley, M.J., van Kranendonk, M.J., Collins, W.J., 2004. Interplay between deformation and magmatism during doming of the Archaean Shaw Granitoid Complex, Pilbara Craton. Western Australia. Precambrian Res. 131, 213–230. https://doi.org/10.1016/j.precamres.2003.12.010.
Petersson, A., Kemp, A.I.S., Whitehouse, M.J., 2019. A Yilgarn seed to the Pilbara Craton (Australia)? Evidence from inherited zircons. Geology 47, 1098–1102. https://doi.org/10.1130/G46696.1.
Petersson, A., Kemp, A.I.S., Gray, C.M., Whitehouse, M.J., 2020. Formation of early Archean Granite-Greenstone Terranes from a globally chondritic mantle: Insights from igneous rocks of the Pilbara Craton. Western Australia. Chemical Geology 551, 119757. https://doi.org/10.1016/j.chemgeo.2020.119757.
Prabhakar, N., Bhattacharya, A., 2013. Paleoarchean partial convective overturn in the Singhbhum Craton, Eastern India. Precambr. Res. 231, 106–121. https://doi.org/10.1016/j.precamres.2013.03.009.
Roberts, N.M., Tikoff, B., Salerno, R.A., 2022. Greenstone-up shear sense at the margin of the Mt Edgar dome, East Pilbara Terrane: Implications for dome and keel formation in the early Earth. Tectonics 1–20. https://doi.org/10.1029/2021tc007042.
Rubatto, D., Burger, M., Lanari, P., Hattendorf, B., Schwarz, G., Neff, C., Keresztes Schmidt, P., Hermann, J., Vho, A., Günther, D., 2020. Identification of growth mechanisms in metamorphic garnet by high-resolution trace element mapping with LA-ICP-TOFMS. Contrib. Miner. Petrol. 175 https://doi.org/10.1007/s00410-020-01700-5.
Salerno, R., Vervoort, J., Fisher, C., Kemp, A., Roberts, N., 2021. The coupled Hf-Nd isotope record of the early Earth in the Pilbara Craton. Earth Planet. Sci. Lett. 572 (August), 117139 https://doi.org/10.1016/j.epsl.2021.117139.
Sandiford, M., Van Kranendonk, M.J., Bodorkos, S., 2004. Conductive incubation and the origin of dome-and-keel structure in Archean granite-greenstone terrains: A model based on the eastern Pilbara Craton, Western Australia. Tectonics 23, 1–19. https://doi.org/10.1029/2002TC001452.
Scherer, E.E., Cameron, K.L., Blichert-Toft, J., 2000. Lu-Hf garnet geochronology: Closure temperature relative to the Sm-Nd system and the effects of trace mineral inclusions. Geochim. Cosmochim. Acta. 64, 3413–3432. https://doi.org/10.1016/S0016-7037(00)00440-3.
Scherer, E.E., Münker, C., Mezger, K., 2001. Calibration of the Lutetium-Hafnium clock. Science 293, 683–687. https://doi.org/10.1126/science.1061372.
Sharp, D.H., 1984. An overview of Rayleigh-Taylor instability. Physica D 12, 3–18. https://doi.org/10.1016/0167-2789(84)90510-4.
Sizova, E., Gerya, T., Brown, M., Stüwe, K., 2018. What drives metamorphism in early Archean greenstone belts? Insights from numerical modeling. Tectonophysics 746, 587–601. https://doi.org/10.1016/j.tecto.2017.07.020.
Smithies, R.H., Van Kranendonk, M.J., Champion, D.C., 2005. It started with a plume - Early Archaean basaltic proto-continental crust. Earth Planet. Sci. Lett. 238, 284–297. https://doi.org/10.1016/j.epsl.2005.07.023.
Smithies, R.H., Champion, D.C., Van Kranendonk, M.J., Hickman, A.H., 2007. Geochemistry of volcanic units of the northern Pilbara Craton. Western Australia, Geological Survey of Western Australia.
Söderlund, U., Patchett, P.J., Vervoort, J.D., Isachsen, C.E., 2004. The 176Lu decay constant determined by Lu-Hf and U-Pb isotope systematics of Precambrian mafic intrusions. Earth Planet. Sci. Lett. 219, 311–324. https://doi.org/10.1016/S0012-821X(04)00012-3.
Spear, F., 1993. Metamorphic Phase Equilibria and Pressure-Temperature-Time Paths. Mineralogical Society of America, Washington DC, USA, p. 799.
Spear, F.S., Kohn, M.J., 1996. Trace element zoning in garnet as a monitor of crustal melting. Geology 24, 1099–1102. https://doi.org/10.1130/0091-7613(1996)024<1099:TEZIGA>2.3.CO;2.
Spry, A., 1969. Metamorphic textures. Pergamon, Oxford UK, p. 350.
Sweetapple, M.T., Collins, P.L.F., 2002. Genetic Framework for the Classification and Distribution of Archean Rare Metal Pegmatites in the North Pilbara Craton, Western Australia. Econ. Geol. 97, 873–895. https://doi.org/10.2113/gsecongeo.97.4.873.
Thébaud, N., Rey, P., 2013. Archean gravity-driven tectonics on hot and flooded continents: Controls on long-lived mineralised hydrothermal systems away from continental margins. Precambrian Res. 229, 93–104. https://doi.org/10.1016/j.precamres.2012.03.001.
Thorpe, R.I., Hickman, A.H., Davis, D.W., Mortensen, J.K., Trendall, A.F., 1992. U-Pb zircon geochronology of Archaean felsic units in the Marble Bar region, Pilbara Craton. Western Australia. Precambrian Res. 56, 169–189. https://doi.org/10.1016/0301-9268(92)90100-3.
Tympel, J.F., Hergt, J.M., Maas, R., Woodhead, J.D., Greig, A., Bolhar, R., Powell, R., 2021. Mantle-like Hf and Nd isotope signatures in ~3.5 Ga greenstones: No evidence for Hadean crust beneath the East Pilbara Craton. Chem. Geol. 576 https://doi.org/10.1016/j.chemgeo.2021.120273.
van Breemen, O., Hawkesworth, C.J., 1980. Sm-Nd isotopic study of garnets and their metamorphic host rocks. In Transactions of the Royal Society of Edinburgh: Earth Sciences 71, 97–102.
Van Kranendonk, M.J., Hickman, A.H., Smithes, R.H., Nelson, D.R., 2002. Geology and tectonic evolution of the Archean North Pilbara Terrain, Pilbara Craton, Western Australia. Econ. Geol. 97, 695–732. https://doi.org/10.2113/gsecongeo.97.4.695.
Van Kranendonk, M.J., Collins, W.J., Hickman, A., Pawley, M.J., 2004. Critical tests of vertical vs. horizontal tectonic models for the Archaean East Pilbara Granite-Greenstone Terrane, Pilbara Craton. Western Australia. Precambrian Res. 131, 173–211. https://doi.org/10.1016/j.precamres.2003.12.015.
Van Kranendonk, M.J., Hickman, A., Smithies, R., Williams, I.R., Farrell, T., 2006. Revised Lithostratigraphy of Archean Supracrustal and Intrusive Rocks in the Northern Pilbara Craton, Western Australia Archean Supracrustal and Intrusive Rocks in the Northern. Geol. Surv. West. Aust. Record 200.
Van Kranendonk, M.J., Hugh Smithies, R., Hickman, A.H., Champion, D.C., 2007. Review: Secular tectonic evolution of Archean continental crust: interplay between horizontal and vertical processes in the formation of the Pilbara Craton. Australia. Terra Nov. 19, 1–38. https://doi.org/10.1111/j.1365-3121.2006.00723.x.
White, A.J.R., Chappell, B.W., 1983. Granitoid Types and Their Distribution in the Lachlan Fold Belt, Southeastern Australia. Geol. Soc. Am. Mem. 159, 21–34. https://doi.org/10.1130/MEM159-p21.
Wickman, F.E., Aberg, G., Levi, B., 1983. Contributions to Mineralogy and Petrology Rb-Sr Dating of Alteration Events in Granitoids. In Contrib Mineral Petrol 83, 358–362.
Wiemer, D., Schrank, C.E., Murphy, D.T., Wenham, L., Allen, C.M., 2018. Earth's oldest stable crust in the Pilbara Craton formed by cyclic gravitational overturns. Nat. Geosci. 11, 357–361. https://doi.org/10.1038/s41561-018-0105-9.
Williams, I. R., Bagas, L., 2007. Geological Survey of Western Australia., Australia. Division of National Mapping., & Geological Survey of Western Australia., Geology of the Mount Edgar 1:100 000 sheet. Geological Survey of Western Australia.
Williams, I.S., Collins, W.J., 1990. Granite-greenstone terranes in the Pilbara Block, Australia, as coeval volcano-plutonic complexes; evidence from U-Pb zircon dating of the Mount Edgar Batholith. Earth Planet. Sci. Lett. 97, 41–53. https://doi.org/10.1016/0012-821X(90)90097-H.
Yardley, B., McKenzie, W., Guilford, C., 1990. Atlas of Metamorphic rocks and their textures. Longman, Essex UK, p. 120.
Zegers, T.E., De Keijzer, M., Passchier, C.W., White, S.H., 1998. The Mulgandinnah Shear zone; an Archean crustal scale strike-slip zone, eastern Pilbara. Western Australia. Precambrian Res. 88, 233–247. https://doi.org/10.1016/s0301-9268(97)00070-3.